
DIVNOISING: Diversity Denoising with Fully Convolutional Variational Autoencoders

Mangal Prakash*

Center for Systems Biology Dresden (CSBD) and
Max-Planck Institute of Molecular Cell Biology and Genetics, Dresden, Germany and
prakash@mpi-cbg.de

Alexander Krull*†

Center for Systems Biology Dresden (CSBD) and
Max-Planck Institute of Molecular Cell Biology and Genetics, Dresden, Germany and
krull@mpi-cbg.de

Florian Jug†

Center for Systems Biology Dresden (CSBD) and
Max-Planck Institute of Molecular Cell Biology and Genetics, Dresden, Germany and
Fondazione Human Technopole, Milano, Italy
jug@mpi-cbg.de, florian.jug@fht.org

Abstract

Deep Learning based methods have emerged as the indisputable leaders for virtually all image restoration tasks. Especially in the domain of microscopy images, various content-aware image restoration (CARE) approaches are now used to improve the interpretability of acquired data. But there are limitations to what can be restored in corrupted images, and any given method needs to make a sensible compromise between many possible clean signals when predicting a restored image. Here, we propose DIVNOISING — a denoising approach based on fully-convolutional variational autoencoders, overcoming this problem by predicting a whole distribution of denoised images. Our method is unsupervised, requiring only noisy images and a description of the imaging noise, which can be measured or bootstrapped from noisy data. If desired, consensus predictions can be inferred from a set of DIVNOISING predictions, leading to competitive results with other unsupervised methods and, on occasion, even with the supervised state-of-the-art. DIVNOISING samples from the posterior enable a plethora of useful applications. We are *(i)* discussing how optical character recognition (OCR) applications could benefit from diverse predictions on ambiguous data, and *(ii)* show in detail how instance cell segmentation gains performance when using diverse DIVNOISING predictions.

*Shared first authors.

†Shared last authors.

1 Introduction

The goal of scientific image analysis is to analyze pixel-data and measure the properties of objects of interest in images. Pixel intensities are subject to undesired noise and other distortions, motivating an initial preprocessing step called *image restoration*. Image restoration is the task of removing unwanted noise and distortions, giving us clean images that are closer to the true but unknown signal.

In the past years, Deep Learning (DL) has enabled tremendous progress in image restoration [1, 2, 3, 4]. Supervised DL methods use corresponding pairs of clean and distorted images to learn a mapping between the two quality levels. The utility of this approach is especially pronounced for microscopy image data of biological samples [5, 4, 6, 7, 8], where quantitative downstream analysis is essential.

Recently, unsupervised content-aware image restoration (CARE) methods [9, 10, 11] have emerged. They can, enabled by sensible assumptions about the statistics of imaging noise, learn a mapping from noisy to clean images, without ever seeing clean data during training. Some of these methods additionally include a probabilistic model of the imaging noise [12, 13, 14, 15] to further improve their performance. Note that such denoisers can directly be trained on a given body of noisy images without requiring additional training data.

All existing approaches have a common flaw: distortions degrade some of the information content in images, generally making it impossible to fully recover the desired clean signal with certainty. Even an ideal method cannot know which of many possible clean images really has given rise to the degraded observation at hand. Hence, any restoration method has to make a compromise between possible solutions when predicting a restored image.

Here we propose DIVNOISING, a fundamentally new image denoising paradigm (see Fig. 1). Instead of committing to a single prediction, our approach allows us to sample diverse solutions from an approximate posterior of possible true signals. To achieve this, we use a fully-convolutional variational autoencoder [16, 17] (VAE). Note that this task is fundamentally different from the *denoising VAEs* introduced in [18] (see Supplementary Material). While other denoising methods [12, 13, 14, 15] predict an independent posterior distribution of intensities for each pixel, DIVNOISING is the first method that learns to approximate the posterior over meaningful structures in given images.

We show that our method achieves visually diverse and convincing results for various datasets. Figure 2 gives an impression of our denoising experiments and results. Additionally, DIVNOISING also allows us to combine our samples to form point estimates (see Fig. 3). Finally, we discuss the utility of diverse denoising results for OCR and showcase it for a ubiquitous analysis task in biology – the instance segmentation of cells in microscopy images (see Fig. 4).

DIVNOISING can be trained fully unsupervised, requiring only a body of noisy images and a suitable model of the imaging noise. Such noise models can also be derived (bootstrapped) from the raw image data alone [12, 14]. Hence, we believe the DIVNOISING approach has the potential to be useful for many real-world applications and will not only generate state-of-the-art restored images, but also enrich quantitative downstream processing pipelines.

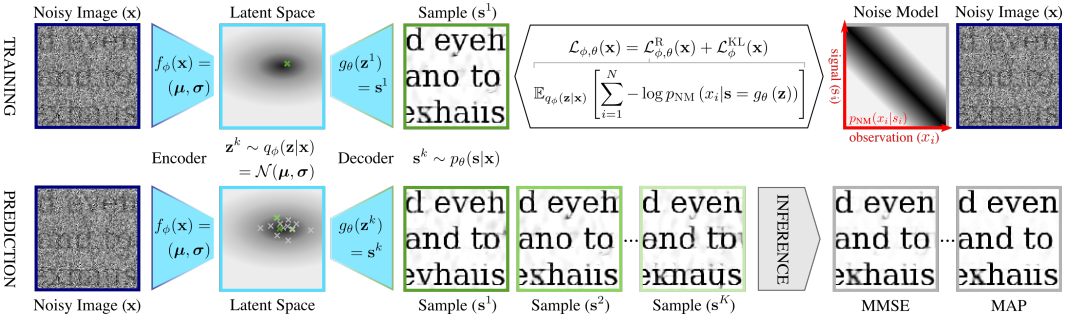


Figure 1: **Training and prediction/inference with DIVNOISING.** (top) A DivNoising VAE can be trained fully unsupervised, using only noisy data and a pixel noise model $p_{NM}(x_i|s_i)$, which can either be measured beforehand, or bootstrapped from noisy data (see main text for details). (bottom) After training, the encoder can be used to sample multiple $\mathbf{z}^k \sim q_\phi(\mathbf{z}|\mathbf{x})$, which are then decoded to denoised samples s^k . These samples can be used to infer point estimates such as MMSE or MAP.

2 The Denoising Task

More formally, image restoration is the task of estimating a clean signal $\mathbf{s} = (s_1, \dots, s_N)$ from a corrupted observation $\mathbf{x} = (x_1, \dots, x_N)$, where s_i and x_i , refer to the respective pixel intensities in both images. The corrupted \mathbf{x} is thought to be drawn from a probability distribution $p_{\text{NM}}(\mathbf{x}|\mathbf{s})$, which we call the *observation likelihood* or the *noise model*. In this work we focus on the restoration of image noise inflicted by limited illumination and detector/camera imperfections³. We cannot hope to exactly derive the true signal from a corrupted observation and we have to admit some uncertainty about the true underlying signal. We will refer to the distribution describing this uncertainty as the *posterior* $p(\mathbf{s}|\mathbf{x})$.

Most existing state-of-the-art denoising methods (e.g. [3, 4]), use paired training data $(\mathbf{x}^j, \mathbf{s}^j)$ to effectively regress the center of mass of the posterior $\mathbb{E}_{p(\mathbf{s}|\mathbf{x})}[\mathbf{s}]$. Note that this is also the estimate that will minimize the expected squared error (MMSE).

We propose, in contrast, to describe the full posterior distribution that captures the remaining uncertainty for a noisy image, while still allowing us to derive the MMSE or other consensus estimates during test time. The posterior we are interested in, namely $p(\mathbf{s}|\mathbf{x}) \propto p(\mathbf{x}|\mathbf{s})p(\mathbf{s})$, depends on two components: the *prior* distribution $p(\mathbf{s})$ of the signal as well as the observation likelihood $p_{\text{NM}}(\mathbf{x}|\mathbf{s})$ we introduced above. While the prior is a highly complex distribution, the likelihood $p(\mathbf{x}|\mathbf{s})$ of a given imaging system (camera/microscope) can be measured and described analytically.

Models of Imaging Noise. The noise model is usually thought to factorize as a product of pixels, implying that the corruption, given the underlying signal, is occurring independently in each pixel

$$p(\mathbf{x}|\mathbf{s}) = \prod_i^N p_{\text{NM}}(x_i|s_i). \quad (1)$$

This assumption is known to hold true for Poisson shot noise and camera readout noise [19, 12, 14]. We will refer to the probability $p_{\text{NM}}(x_i|s_i)$ of observing a particular noisy value x_i at a pixel i given clean signal s_i as the *pixel noise model*. Various types of pixel noise models have been proposed, ranging from physics based analytical models [19, 20, 21] to simple histograms [12] that explicitly describe the distribution of noisy observations for each possible clean signal. In this work, we follow the Gaussian Mixture Model (GMM) based noise model description of [14]. The parameters of a noise model can be estimated whenever pairs $(\mathbf{x}', \mathbf{s}')$ of corresponding noisy and clean calibration images are available. In a microscopy setting, such calibration data can easily be derived by repeatedly imaging a stationary sample, producing noisy observations \mathbf{x}^{tj} . The signal $\mathbf{s}' \approx \frac{1}{M} \sum_{j=0}^M \mathbf{x}^{tj}$ can then be computed by averaging these noisy observations [14].

In a case where no calibration data can be acquired, \mathbf{s}' can be estimated by a simple bootstrapping approach. Using an unsupervised denoising method that does not require a noise model (e.g. N2V [10]), denoised images can be predicted and used to generate a suitable noise model [14, 15].

3 The Variational Autoencoder (VAE) Setup

Here, we want to give a very brief overview of the VAE approach introduced by Kingma *et al.* in [16]. A more complete discussion can be found in [22]. VAEs are generative models, capable of learning complex distributions over classes of images \mathbf{x} , such as hand written digits [16] or faces [23]. To achieve this, VAEs use a latent variable \mathbf{z} and describe

$$p_{\theta}(\mathbf{x}) = \int p_{\theta}(\mathbf{x}|\mathbf{z})p(\mathbf{z})d\mathbf{z}. \quad (2)$$

Like conventional autoencoders, they consist of two components: an *encoder* network $f_{\phi}(\mathbf{x})$, which takes an observed image and maps it to the latent space, and a *decoder* network $g_{\theta}(\mathbf{z})$ that implements the inverse operation. By ϕ and θ we denote network parameters of the encoder and decoder, respectively. Next, we will take a closer look at the model from Eq. 2.

³While we are not targeting other degradations like motion blur or diffraction artifacts, future variations of DIVNOISING might address such distortions.

The Generative Model. In VAEs the latent variable \mathbf{z} is defined to follow a multivariate unit normal distribution $p(\mathbf{z})$. The decoder describes the conditional probability $p_\theta(\mathbf{x}|\mathbf{z})$ of observing \mathbf{x} , given the latent variable \mathbf{z} . It is assumed to factorize as

$$p_\theta(\mathbf{x}|\mathbf{z}) = \prod_{i=1}^N p_\theta(x_i|\mathbf{z}), \quad (3)$$

where $p_\theta(x_i|\mathbf{z})$ is the distribution of a pixel intensity given the latent vector. It is often modelled as a normal distribution, with the parameters for each pixel i predicted by the decoder network. Together with $p(\mathbf{z})$, our decoder completely describes the model in Eq. 2.

Training. The goal is to find decoder parameters, such that Eq. 2 well describes the distribution of training images $\mathbf{x}^1 \dots \mathbf{x}^M$. To enable this training task, the VAE relies on its encoder. The encoder describes a distribution $q_\phi(\mathbf{z}|\mathbf{x})$, aiming to approximate the distribution of the latent variable given the image, as it is implicitly defined by the decoder

$$q_\phi(\mathbf{z}|\mathbf{x}) \approx p_\theta(\mathbf{z}|\mathbf{x}) = \frac{p_\theta(\mathbf{x}|\mathbf{z})p(\mathbf{z})}{\int p_\theta(\mathbf{x}|\mathbf{z}')p(\mathbf{z}')d\mathbf{z}'}. \quad (4)$$

The encoder describes its distribution as a product over the D -dimensional latent variable

$$q_\phi(\mathbf{z}|\mathbf{x}) = \prod_{i=1}^D q_\phi(z_i|\mathbf{x}), \quad (5)$$

with $q_\phi(z_i|\mathbf{x}) = \mathcal{N}(\mu_i, \sigma_i)$ denoting the distribution for an element i of the latent space. The means and standard deviations for each element are predicted by the encoder network $f_\phi(\mathbf{x}) = (\boldsymbol{\mu}, \boldsymbol{\sigma}) = (\mu_1 \dots \mu_D, \sigma_1 \dots \sigma_D)$. Based on this setup, both networks are trained jointly by optimizing the loss

$$\mathcal{L}_{\phi, \theta}(\mathbf{x}) = \mathcal{L}_{\phi, \theta}^{\text{R}}(\mathbf{x}) + \mathcal{L}_{\phi}^{\text{KL}}(\mathbf{x}), \quad (6)$$

where

$$\mathcal{L}_{\phi, \theta}^{\text{R}}(\mathbf{x}) = \mathbb{E}_{q_\phi(\mathbf{z}|\mathbf{x})}[-\log p_\theta(\mathbf{x}|\mathbf{z})] = \mathbb{E}_{q_\phi(\mathbf{z}|\mathbf{x})} \left[\sum_{i=1}^N -\log p_\theta(x_i|\mathbf{z}) \right], \quad (7)$$

and $\mathcal{L}_{\phi}^{\text{KL}}(\mathbf{x})$ is the KL divergence $\mathbb{KL}(q_\phi(\mathbf{z}|\mathbf{x})||p(\mathbf{z}))$. While $\mathcal{L}_{\phi}^{\text{KL}}(\mathbf{x})$ can be computed analytically, the expected value in Eq. 7 is approximated by drawing a single sample \mathbf{z}^1 from $q_\phi(\mathbf{z}|\mathbf{x})$ and using the *reparametrization trick* [16] for gradient computation. It has been shown in [16] that minimizing Eq. 6 simultaneously achieves two goals: (i) the model defined by the decoder well describes the distribution of the observed data, and (ii) the encoder gives a good approximation of Eq. 4.

Image Generation. Once trained, images from $p_\theta(\mathbf{x})$ can be generated by drawing samples $\mathbf{z}^k \sim p(\mathbf{z})$ from the normal distribution in latent space and processing them with the decoder to sample the pixel values from $x_i^k \sim p_\theta(x_i|\mathbf{z}^k)$.

Fully Convolutional Architecture. Originally, VAEs were using fully connected network architectures, or a mixture of convolutional and fully connected layers. Such architectures can only process fixed size inputs. However, recently the use of fully convolutional VAE architectures was proposed [17]. In our work, we also use a fully convolutional architecture (see Section 5), enabling us to process arbitrarily sized input images.

4 DivNoising

In DIVNOISING, we use the VAE setup described in the previous section. However, we interpret VAEs from a denoising-specific perspective. We assume that the observed images have been created from a clean signal \mathbf{s} via a known noise model, i.e., $\mathbf{x} \sim p_{\text{NM}}(\mathbf{x}|\mathbf{s})$. Based on this, we replace the generic normal distribution over pixel intensities in Eq. 3 with $p_{\text{NM}}(\mathbf{x}|\mathbf{s})$ from Eq. 1. We get

$$p_\theta(\mathbf{x}|\mathbf{z}) = p_{\text{NM}}(\mathbf{x}|\mathbf{s}) = \prod_i^N p_{\text{NM}}(x_i|s_i), \quad (8)$$

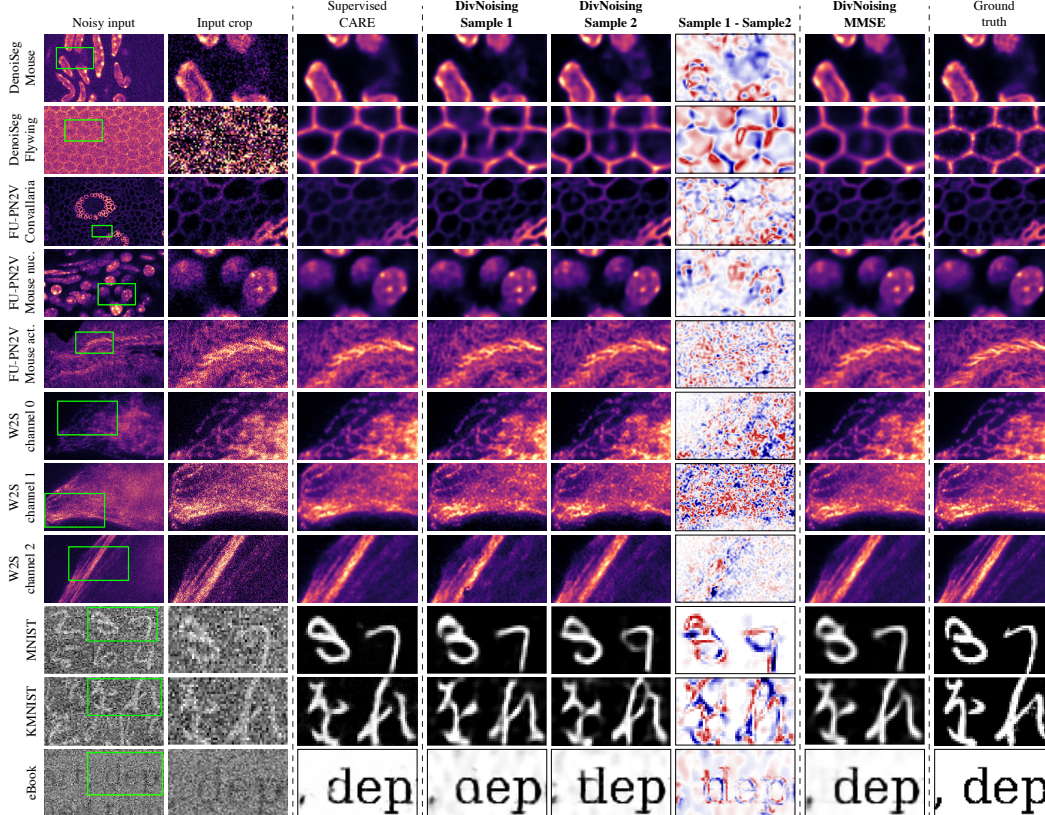


Figure 2: **Qualitative denoising results.** We compare two DIVNOISING samples, the MMSE estimate (derived by averaging 1000 sampled images), and results by the supervised CARE baseline. The diversity between individual samples is visualized in the column of difference images. (See the Supplementary Material for additional images of DIVNOISING results.)

with the decoder now predicting the signal $g_\theta(\mathbf{z}) = \mathbf{s}$. Together with $p(\mathbf{z})$ and the noise model, the decoder now describes a full joint model for all three variables, including the signal:

$$p_\theta(\mathbf{z}, \mathbf{x}, \mathbf{s}) = p_{\text{NM}}(\mathbf{x}|\mathbf{s})p_\theta(\mathbf{s}|\mathbf{z})p(\mathbf{z}), \quad (9)$$

where we assume that $p_{\text{NM}}(\mathbf{x}|\mathbf{s}, \mathbf{z}) = p_{\text{NM}}(\mathbf{x}|\mathbf{s})$. For a given \mathbf{z}^k , as for standard VAEs, the decoder describes a distribution over noisy images $p(\mathbf{x}|\mathbf{z})$. The corresponding clean signal \mathbf{s}^k , in contrast, is deterministically defined. Hence, $p_\theta(\mathbf{s}|\mathbf{z})$ is a Dirac distribution centered at $g_\theta(\mathbf{z})$.

Training. Considering Eq. 1, the reconstruction loss of Eq. 7 becomes

$$\mathcal{L}_{\phi, \theta}^{\text{R}}(\mathbf{x}) = \mathbb{E}_{q_\phi(\mathbf{z}|\mathbf{x})} \left[\sum_{i=1}^N -\log p(x_i|\mathbf{s} = g_\theta(\mathbf{z})) \right]. \quad (10)$$

Apart from this modification, we can follow the standard VAE training procedure, just as described in Section 3. Since we have only modified how the decoder distribution is modeled, we assume that the training procedure still produces (i) a model describing the distribution of our training data, while (ii) making sure that Eq. 4 is well approximated.

Prediction. While we can obviously use the trained VAE to generate images from $p_\theta(\mathbf{x})$ (see Supplementary Material), we are actually mainly interested in denoising and desire access to the posterior $p(\mathbf{s}|\mathbf{x})$, *i.e.* to the distribution of possible clean signals \mathbf{s} given a noisy observed image \mathbf{x} . Assuming the encoder and decoder are sufficiently well trained, they allow us to obtain samples \mathbf{s}^k from an approximate posterior by: (i) feeding the noisy image \mathbf{x} into our encoder, (ii) drawing samples $\mathbf{z}^k \sim q_\phi(\mathbf{z}|\mathbf{x})$, and (iii) decoding the samples via the decoder to obtain $\mathbf{s}^k = g_\theta(\mathbf{z}^k)$.

Inference. Given a set of posterior samples \mathbf{s}^k for a noisy image \mathbf{x} , we can infer different consensus estimates for high-quality denoised images. We can, for example, approximate the MMSE estimate (see Fig. 2), by averaging many samples \mathbf{s}^k .

Alternatively, we can attempt to find the *maximum a posteriori* (MAP) estimate, *i.e.* the most likely signal given the noisy observation \mathbf{x} . This corresponds to the mode of the posterior distribution. For this purpose, we iteratively use the mean shift algorithm [24] with decreasing bandwidth to find the mode of our sample set (see Fig. 3 and Supplementary Material).

Nevertheless, being able to sample from the posterior is useful. Instead of committing to a consensus estimate, diverse samples \mathbf{s}^k can directly be used. Any downstream processing pipeline that can benefit from diverse hypotheses can benefit from DIVNOISING samples from $p(\mathbf{s}|\mathbf{x})$. In Section 5, we give a full instance segmentation example and discuss the potential of DIVNOISING for OCR applications.

5 Data, Experiments, Results

We evaluated the performance of DIVNOISING on 9 publicly available datasets, 4 of which are subject to a high level of intrinsic noise. To 5 others we have synthetically added noise, hence giving us full knowledge about the nature of the added noise.

Data Exposed to Synthetic Noise. We use the well known *MNIST* [25] as well as the *KMNIST* [26] dataset showing 28×28 images of handwritten digits and phonetic letters of hiragana, respectively. Both datasets contain 60000 training examples and 10000 test examples. Onto both datasets we added pixel-wise independent Gaussian noise with $\mu = 0$ and $\sigma = 140$. As a third text-based dataset we rendered the freely available *eBook* “The Beetle” [27] and extracted 40800 image patches of size 128×128 . We separated 34680 patches for training and 6120 patches for validation, and added pixel-wise independent Gaussian noise with $\mu = 0$ and $\sigma = 255$. Additionally, we use two datasets from microscopy. The *DenoiSeg Mouse* [28] data, showing cell nuclei in the developing mouse skull, consists of 908 training and 160 validation images of size 128×128 , with additional 67 images of size 256×256 for testing. All images were exposed to pixel-wise independent Gaussian noise with $\mu = 0$ and $\sigma = 20$. Lastly, the *DenoiSeg Flywing* [28] data is showing membrane labeled cells in a fly wing, consisting of 1428 training and 252 validation patches of size 128×128 , with additional 42 images of size 512×512 for testing. We exposed this data to pixel-wise independent Gaussian noise with $\mu = 0$ and $\sigma = 70$ to create a synthetic low SNR version. All original datasets are 8-bit.

Intrinsically Noisy Microscopy Data. We use 4 public microscopy datasets which show realistic levels of noise, introduced by the respective optical imaging setups. The *FU-PN2V Convallaria* [12, 14] data, consists of 100 noisy calibration images (intended to generate a noise model), and 100 images of size 1024×1024 showing a noisy *Convallaria* section. The *FU-PN2V Mouse nuclei* [14] data is composed of 500 noisy calibration images and 200 noisy images of size 512×512 showing labeled cell nuclei. The *FU-PN2V Mouse actin* [14] data from the same source consists of 100 noisy calibration images and 100 noisy images of size 1024×1024 of the same sample, but labeled for the protein actin. Finally, we use all 3 channels of 2 noise levels (avg1 and avg16) of the *W2S* [29] data. For each channel, corresponding high quality (ground truth) images are available. Each channel’s training and test sets consist of 80 and 40 images, respectively. All images are 512×512 pixels in size. Here we used the original raw data made available to us by the authors of [29], since their pre-released 8-bit dataset is inconsistently scaled. Hence, results we report here must not be compared to the ones reported in their preprint [29].

Denoising Baselines. We choose state-of-the-art baseline methods to compare against DIVNOISING, namely, the supervised CARE [4] and the unsupervised methods NOISE2VOID (N2V) [10] and Probabilistic NOISE2VOID (PN2V) [10]. All baselines use the available implementations of [12] and, as long as not specified otherwise, make use of a depth 3 U-NET with 1 input channel and 64 channels in the first layer. Training is performed using the ADAM [30] optimizer for 200 epochs (5 steps per epoch for CARE and PN2V and 10 steps per epoch for N2V) with a batch size of 1 and a virtual batch size of 20, an initial learning rate of 0.001, and the same basic learning rate scheduler as in [12]. All baselines use on the fly data augmentation (flipping and rotation) during training.

Training details. In all experiments we use rather small, fully convolutional VAE networks, with either 200k or 713k parameters (see Supplementary Material). For all experiments on intrinsically noisy microscopy data, validation and test set splits follow the ones described in the respective publication. In contrast to the synthetically noisy data, no apriori noise model is known for microscopy datasets. Still, for *FU-PN2V Convallaria*, *FU-PN2V Mouse nuclei*, and *FU-PN2V Mouse actin*, suitable noise models have previously been created [12, 14, 15], and we have used the GMM-based

Dataset	Unsupervised			Supervised	
	N2V	PN2V	DivNoising (MMSE)	CARE	
DenoiseSeg	Mouse	33.55	34.19	34.03	34.63
	Flywing	22.85	24.85	25.10	25.60
FU-PN2V	Convallaria	35.73	36.47	36.94	36.71
	Convallaria (bootstr.)	35.73	36.70	36.63	36.71
	Mouse Actin	33.39	33.86	33.98	34.20
	Mouse Nuclei	35.84	36.35	36.31	36.58
W2S	Ch. 0 (avg1)	34.36	-	34.13	34.30
	Ch. 1 (avg1)	31.96	-	32.28	32.11
	Ch. 2 (avg1)	34.78	32.48	35.18	34.73
	Ch. 0 (avg16)	38.83	39.19	39.62	41.94
	Ch. 1 (avg16)	37.80	38.24	38.37	39.09
	Ch. 2 (avg16)	40.17	40.49	40.52	40.88

Table 1: **Quantitative denoising results of DIVNOISING and our baseline methods.** We compare all results in terms of Peak Signal-to-Noise Ratio (PSNR in dB) to available high quality (clean) images. We highlight the best performing method by an underline and the best unsupervised method in bold. The missing PN2V baseline values are caused by numeric instabilities during training. Our results are typically on par or better than the unsupervised baselines. In 3 out of 12 cases we even improve on supervised CARE results.

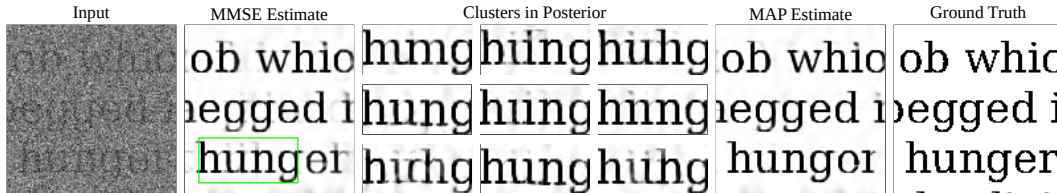


Figure 3: **A closer look at the learned posterior distribution of possible clean signals.** We show results for the eBook dataset. The MMSE estimate (10k averaged samples) contains compromises (faintly overlaid letters), a consequence of ambiguities in the input image. We perform mean shift clustering on a cropped version of sampled images to obtain local high density points in our samples from the posterior. We show the 9 clusters with the highest support in no particular order. Additionally, we obtain an approximate MAP estimate (Supplementary Material), which removes most artifacts visible in the MMSE solution.

noise model approach of [14] to recreate them. For the *W2S* datasets, no dedicated calibration samples to create noise models are available. Hence, for all experiments on this dataset, we use the available clean ground truth images and all noisy observations of the training data to learn a GMM-based noise model. For all noise models we are using 3 Gaussians and 2 coefficients each. Find more details in the Supplementary Material.

Denoising Results. In Table 1, we report denoising performance of all experiments we conducted in terms of peak signal-to-noise ratio (PSNR) with respect to available ground truth images. Our results show that denoising results of DIVNOISING (using the inferred MMSE estimate with 1000 samples) are typically either on par or even beyond the denoising quality reached by the unsupervised baselines. While DIVNOISING MMSE is typically, as expected, slightly behind the performance of the fully supervised baseline CARE [4], in 3 of our 12 experiments on microscopy data we have even outperformed it. Additionally, on *FU-PN2V Convallaria* we have demonstrated that a suitable noise model for DIVNOISING can be created via bootstrapping [14, 15].

Downstream Processing: OCR. In Fig. 3 we show how Optical Character Recognition (OCR) applications might benefit from diverse denoising hypotheses. While regular denoising approaches predict poor compromises that would never be seen in clean text documents (multiple faintly overlaid letters), DIVNOISING can generate a diverse set of rather plausible denoised solutions. While our MAP estimate cleans up most of the problems, it cannot avoid occasionally making mistakes, *e.g.* changing "hunger" to "hungor" (see Fig. 3). We used clustering to identify diverse denoising solutions and find that they, albeit still on occasion containing faint artefacts, typically correspond to plausible alternative interpretations. It stands to reason that OCR systems could benefit in various ways from having access to such diverse interpretations.

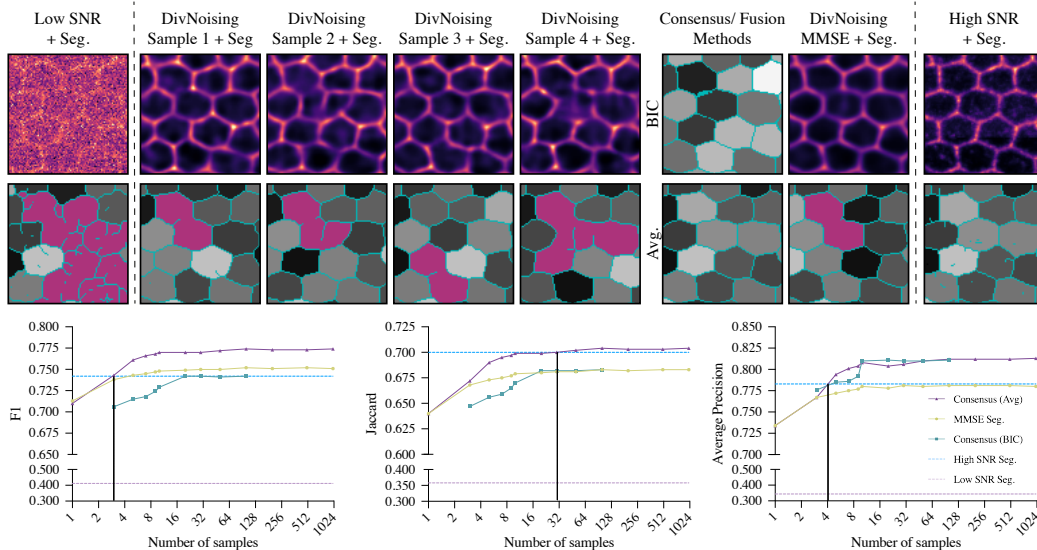


Figure 4: **DivNoising enables downstream segmentation tasks.** (*top*) We show various cell segmentation results as well as the corresponding denoised images they were produced from. Cells that were segmented incorrectly (merged or split) are indicated in magenta. Sampled DIVNOISING results give rise to diverse segmentation hypotheses. (*bottom*) We quantitatively evaluate the quality of the different segmentation results using the F1 score [31], Jaccard score [32] and Average Precision [33]. On the x-axis, we depict the number of samples/labels used by any given method. The performance of BIC is only evaluated up to 100 samples because of run time constraints (setting an upper time limit of 30 minutes). Remarkably, *Consensus (Avg)*, even using as little as 30 DIVNOISING segmentation labels, outperforms segmentations obtained from high SNR images on all available metrics.

Downstream Processing: Instance Cell Segmentation. We demonstrate how diverse denoised images generated with DIVNOISING can help to segment all cells in the *DenoiSeg Flying* data. While methods to generate diverse segmentations do exist [34, 35], they require ground truth segmentation labels during training. In contrast, we use a simple and fast downstream segmentation pipeline $c(x)$ based on local thresholding and skeletonization (see Supplementary Material for details) and apply it to individual samples ($s^1 \dots s^K$) predicted by DIVNOISING to derive segmentations ($c^1 \dots c^K$). We explore two label fusion methods to combine the individual results and obtain an improved segmentation. We do: (i) use *Consensus (BIC)* [36] and (ii) create a pixel-wise average of ($c^1 \dots c^K$), followed by again applying our threshold based segmentation procedure on this average, calling it *Consensus (Avg)*.

For comparison, we also segment (i) the low SNR input images, (ii) the original high SNR microscopy images, and (iii) the MMSE solutions of DIVNOISING. Figure 4 shows all results of our instance segmentation experiments. It is important to note that segmentation from even a single DIVNOISING prediction outperforms segmentations on the low SNR image data by a large margin. We observe that label fusion methods can, by utilizing multiple samples, outperform the MMSE estimate, with *Consensus (Avg)* giving the best overall results.

6 Discussion and Conclusion

We have introduced DIVNOISING, a novel unsupervised denoising paradigm that allows us, for the first time, to generate diverse and plausible denoising solutions, sampled from a learned posterior. We have demonstrated that the quality of denoised images is highly competitive, typically outperforming the unsupervised state-of-the-art, and at times even improving on supervised results.⁴

We find that DIVNOISING is suited particularly well for microscopy data or other applications on a limited image domain. In its current form it works less well on collections of natural images (see Supplementary Material). We do not think this is very surprising, as we are training a generative

⁴ Supervised methods trained on perfect ground truth should outperform DIVNOISING. Still, ground truth is also subject to imperfections, at times leading to inferior results.

model for our image data and would not expect to be capturing the tremendously diverse domain of natural photographic images with the comparatively tiny networks used in our experiments (see Supplementary Material). For microscopy data, instead, the diversity between datasets can be huge. Images of the same type of sample, acquired using the same experimental setup, however, typically contain many resembling structures of lesser overall diversity (they are from a limited image domain). Nevertheless, the stunning results we achieve suggest that DIVNOISING will also find application in other areas where low SNR limited domain image data has to be analyzed. Next to microscopy, we can think of astronomy, medical imaging, or limited domain natural images such as faces or street scenes. Additionally, follow up research will explore larger and improved network architectures, able to capture more complex DIVNOISING posteriors on datasets covering larger image domains.

While we constrained ourselves to the standard per-pixel noise models in this paper, the DIVNOISING approach could in principle also work with more sophisticated higher level image degradation models, as long as they can be probabilistically described. This might include diffraction, blur or even compression and demosaicing artefacts.

Maybe most importantly, DIVNOISING can not only produce competitive and diverse results, but these results can also be leveraged for downstream processing. We have seen that cell segmentation can be improved and that clustering our results provides us with meaningful alternative interpretations of the same data (see Fig. 3). We believe that this is a highly promising direction for many applications, as it provides us with a way to account for the uncertainty introduced by the imaging process. We are looking forward to see how DIVNOISING will be applied and extended by the community, showcasing the true potential and limitations of this approach.

Broader Impact

Impact: We believe that our method is particularly well suited for the type of data that is commonly found in biological and medical research labs around the world. These labs do very specialized experiments, each of which produces large amounts of microscopy data that (i) is often acquired at very low light levels in order to protect the sample, (ii) typically the same microscope is used for all images of a given dataset, and (iii) in many cases, plenty of images of similar structures are acquired, meaning that the diversity within each dataset is limited compared to natural images. We will make our software available under a permissive open source license and even plan to integrate it in a widespread and easy to use application. The fact that our method is unsupervised means that it does not require the acquisition of additional training data. Hence, due to availability and applicability we expect DIVNOISING to bring immediate benefit to a huge user-base.

Ethics: The stunning performance of DL-based image restoration methods sparked heated scientific discussions in the microscopy field, with many potential users fearing to introduce ‘invisible’ biases to their measurements. In our opinion, unsupervised methods such as DIVNOISING, which can be trained on the very data to be denoised, can help to avoid two frequent pitfalls, namely (i) training restoration models with training data of insufficient quality, and (ii) having mismatching training and test data, *i.e.* applying a trained model to data from a different domain. Last but not least, DIVNOISING will, by its very nature, educate users about uncertainty in their data. While other methods suggest that a noisy image can unambiguously be restored, DIVNOISING communicates the uncertainty in a given image by generating diverse but plausible samples.

Acknowledgments and Disclosure of Funding

We would like to thank Ruofan Zhou, Majed El Helou and Sabine Suesstrunk from EPFL Lausanne for access to their raw W2S data. Funding was provided from the core budget of the Max Planck Institute of Molecular Cell Biology and Genetics, the Max Planck Institute for Physics of Complex Systems, the BMBF under codes 031L0102 (de.NBI) and 01IS18026C (ScaDS2), and the DFG under code JU3110/1-1 (FiSS). Finally, we would like to thank the Scientific Computing Facility and the Light Microscopy Facility at MPI-CBG for giving us access to their computing and microscopy resources.

References

- [1] Xiaojiao Mao, Chunhua Shen, and Yu-Bin Yang. Image restoration using very deep convolutional encoder-decoder networks with symmetric skip connections. In D. D. Lee, M. Sugiyama, U. V. Luxburg, I. Guyon, and R. Garnett, editors, *Advances in Neural Information Processing Systems 29*, pages 2802–2810. Curran Associates, Inc., 2016.
- [2] Kai Zhang, Wangmeng Zuo, Shuhang Gu, and Lei Zhang. Learning deep cnn denoiser prior for image restoration. In *The IEEE Conference on Computer Vision and Pattern Recognition (CVPR)*, July 2017.
- [3] K. Zhang, W. Zuo, Y. Chen, D. Meng, and L. Zhang. Beyond a gaussian denoiser: Residual learning of deep cnn for image denoising. *IEEE Transactions on Image Processing*, 26(7):3142–3155, 2017.
- [4] Martin Weigert, Uwe Schmidt, Tobias Boothe, Andreas Müller, Alexandr Dibrov, Akanksha Jain, Benjamin Wilhelm, Deborah Schmidt, Coleman Broaddus, Siân Culley, et al. Content-aware image restoration: pushing the limits of fluorescence microscopy. *Nature methods*, 15(12):1090–1097, 2018.
- [5] Martin Weigert, Loïc Royer, Florian Jug, and Gene Myers. Isotropic reconstruction of 3D fluorescence microscopy images using convolutional neural networks. *arXiv*, April 2017.
- [6] Wei Ouyang, Andrey Aristov, Mickaël Elek, Xian Hao, and Christophe Zimmer. Deep learning massively accelerates super-resolution localization microscopy. *Nat Biotechnol*, 27:2672, April 2018.
- [7] Hongda Wang, Yair Rivenson, Yiyin Jin, Zhensong Wei, Ronald Gao, Harun Günaydin, Laurent A Bentolila, Comert Kural, and Aydogan Ozcan. Deep learning enables cross-modality super-resolution in fluorescence microscopy. *Nature Publishing Group*, 16(1):103–110, January 2019.
- [8] Tim-Oliver Buchholz, Alexander Krull, Réza Shahidi, Gaia Pigo, Gáspár Jékely, and Florian Jug. Content-aware image restoration for electron microscopy. In Gaia Pigo and Thomas Müller-Reichert, editors, *Three-Dimensional Electron Microscopy*, pages 277–289. Academic Press, July 2019.
- [9] Jaakko Lehtinen, Jacob Munkberg, Jon Hasselgren, Samuli Laine, Tero Karras, Miika Aittala, and Timo Aila. Noise2noise: Learning image restoration without clean data. *arXiv preprint arXiv:1803.04189*, 2018.
- [10] Alexander Krull, Tim-Oliver Buchholz, and Florian Jug. Noise2void-learning denoising from single noisy images. In *Proceedings of the IEEE Conference on Computer Vision and Pattern Recognition*, pages 2129–2137, 2019.
- [11] Joshua Batson and Loic Royer. Noise2self: Blind denoising by self-supervision, 2019.
- [12] Alexander Krull, Tomas Vicar, Mangal Prakash, Manan Lalit, and Florian Jug. Probabilistic Noise2Void: Unsupervised Content-Aware Denoising. *Front. Comput. Sci.*, 2:60, February 2020.
- [13] Samuli Laine, Tero Karras, Jaakko Lehtinen, and Timo Aila. High-quality self-supervised deep image denoising. In *Advances in Neural Information Processing Systems*, pages 6968–6978, 2019.
- [14] Mangal Prakash, Manan Lalit, Pavel Tomancak, Alexander Krull, and Florian Jug. Fully unsupervised probabilistic noise2void. *arXiv preprint arXiv:1911.12291*, 2019.
- [15] Wesley Khademi, Sonia Rao, Clare Minnerath, Guy Hagen, and Jonathan Ventura. Self-supervised poisson-gaussian denoising. *arXiv preprint arXiv:2002.09558*, 2020.
- [16] Diederik P. Kingma and Max Welling. Auto-encoding variational bayes. In Yoshua Bengio and Yann LeCun, editors, *2nd International Conference on Learning Representations, ICLR 2014, Banff, AB, Canada, April 14-16, 2014, Conference Track Proceedings*, 2014.
- [17] Yaxiang Fan, Gongjian Wen, Deren Li, Shaohua Qiu, Martin D Levine, and Fei Xiao. Video anomaly detection and localization via gaussian mixture fully convolutional variational autoencoder. *Computer Vision and Image Understanding*, page 102920, 2020.

- [18] Daniel Im Jiwoong Im, Sungjin Ahn, Roland Memisevic, and Yoshua Bengio. Denoising criterion for variational auto-encoding framework. In *Thirty-First AAAI Conference on Artificial Intelligence*, 2017.
- [19] Yide Zhang, Yinhao Zhu, Evan Nichols, Qingfei Wang, Siyuan Zhang, Cody Smith, and Scott Howard. A poisson-gaussian denoising dataset with real fluorescence microscopy images. In *CVPR*, 2019.
- [20] Florian Luisier, Thierry Blu, and Michael Unser. Image denoising in mixed poisson–gaussian noise. *IEEE Transactions on image processing*, 20(3):696–708, 2010.
- [21] Alessandro Foi, Mejdí Trimeche, Vladimir Katkovnik, and Karen Egiazarian. Practical poissonian-gaussian noise modeling and fitting for single-image raw-data. *IEEE Transactions on Image Processing*, 17(10):1737–1754, 2008.
- [22] Diederik P. Kingma and Max Welling. An introduction to variational autoencoders. *Foundations and Trends® in Machine Learning*, 12(4):307–392, 2019.
- [23] Huaibo Huang, Ran He, Zhenan Sun, Tieniu Tan, et al. Introvae: Introspective variational autoencoders for photographic image synthesis. In *Advances in neural information processing systems*, pages 52–63, 2018.
- [24] Yizong Cheng. Mean shift, mode seeking, and clustering. *IEEE transactions on pattern analysis and machine intelligence*, 17(8):790–799, 1995.
- [25] Yann LeCun, Léon Bottou, Yoshua Bengio, and Patrick Haffner. Gradient-based learning applied to document recognition. *Proceedings of the IEEE*, 86(11):2278–2324, 1998.
- [26] Tarin Clanuwat, Mikel Bober-Irizar, Asanobu Kitamoto, Alex Lamb, Kazuaki Yamamoto, and David Ha. Deep learning for classical japanese literature. *arXiv preprint arXiv:1812.01718*, 2018.
- [27] Richard Marsh. *The beetle*. Broadview Press, 2004.
- [28] Tim-Oliver Buchholz, Mangal Prakash, Alexander Krull, and Florian Jug. Denoiseg: Joint denoising and segmentation. *arXiv preprint arXiv:2005.02987*, 2020.
- [29] Ruofan Zhou, Majed El Helou, Daniel Sage, Thierry Laroche, Arne Seitz, and Sabine Süsstrunk. W2s: A joint denoising and super-resolution dataset. *arXiv preprint arXiv:2003.05961*, 2020.
- [30] Diederik P Kingma and Jimmy Ba. Adam: A method for stochastic optimization. 3rd international conference on learning representations, iclr 2015. *arXiv preprint arXiv:1412.6980*, 9, 2015.
- [31] Cornelis Joost Van Rijsbergen. *Information retrieval*. Citeseer, 1979.
- [32] Paul Jaccard. Étude comparative de la distribution florale dans une portion des alpes et des jura. *Bull Soc Vaudoise Sci Nat*, 37:547–579, 1901.
- [33] Tsung-Yi Lin, Michael Maire, Serge Belongie, James Hays, Pietro Perona, Deva Ramanan, Piotr Dollár, and C Lawrence Zitnick. Microsoft coco: Common objects in context. In *European conference on computer vision*, pages 740–755. Springer, 2014.
- [34] Simon Kohl, Bernardino Romera-Paredes, Clemens Meyer, Jeffrey De Fauw, Joseph R Led- sam, Klaus Maier-Hein, SM Ali Eslami, Danilo Jimenez Rezende, and Olaf Ronneberger. A probabilistic u-net for segmentation of ambiguous images. In *Advances in Neural Information Processing Systems*, pages 6965–6975, 2018.
- [35] Simon AA Kohl, Bernardino Romera-Paredes, Klaus H Maier-Hein, Danilo Jimenez Rezende, SM Eslami, Pushmeet Kohli, Andrew Zisserman, and Olaf Ronneberger. A hierarchical probabilistic u-net for modeling multi-scale ambiguities. *arXiv preprint arXiv:1905.13077*, 2019.
- [36] Cem Emre Akbas, Vladimír Ulman, Martin Maska, Florian Jug, and Michal Kozubek. Automatic fusion of segmentation and tracking labels. In *Proceedings of the European Conference on Computer Vision (ECCV)*, pages 0–0, 2018.

DIVNOISING: Diversity Denoising with Fully Convolutional Variational Autoencoders

-

Supplementary Material

Mangal Prakash*

Center for Systems Biology Dresden (CSBD) and
Max-Planck Institute of Molecular Cell Biology and Genetics, Dresden, Germany and
prakash@mpi-cbg.de

Alexander Krull*†

Center for Systems Biology Dresden (CSBD) and
Max-Planck Institute of Molecular Cell Biology and Genetics, Dresden, Germany and
krull@mpi-cbg.de

Florian Jug†

Center for Systems Biology Dresden (CSBD) and
Max-Planck Institute of Molecular Cell Biology and Genetics, Dresden, Germany and
Fondazione Human Technopole, Milano, Italy
jug@mpi-cbg.de, florian.jug@fht.org

1 Training and Network Details

Here, we provide additional details about the network architecture and training parameters used throughout the main manuscript. For all DIVNOISING experiments, we use rather lightweight depth 2 and depth 3 VAE architectures (see Supplementary Figs. 1 and 2, respectively). All networks use a single input channel and 32 feature channels in the first network layer. We use two 3×3 convolutions (with padding 1), each followed by ReLU activation, followed by a 2×2 max pooling layer. After each such downsampling step, we double the number of feature channels. For all experiments we use a network architecture of depth 2 (with 2 down/upsampling steps). The only exceptions are our experiments on *DenoiSeg Flywing* and *eBook* data, for which we use a depth 3 architecture (with 3 down/upsampling steps). In total, our depth 2 networks have only around $200k$ parameters and depth 3 networks have around $700k$ parameters.

While we generally use a VAE bottleneck of 64 latent space feature dimensions for each pixel of the image (after encoding), for the small 28×28 MNIST and KMNIST images we use only 8 such latent space dimensions.

We consistently use 8-fold data augmentation (rotation and flipping) in all experiments. All networks are trained with a batch size of 32 and an initial learning rate of 0.001. The learning rate is multiplied by 0.5 if the validation loss does not decrease for 30 epochs.

For all datasets other than MNIST and KMNIST, we extract training patches of size 128×128 , and separate 15% of all patches for validation. We set the maximum number of epochs such that

*Shared first authors.

†Shared last authors.

approximately 22 million steps are performed, and in each epoch the entire training data is being fed. Training is terminated if the validation loss does not decrease by at least 10^{-6} over 100 epochs.

For *DenoiSeg Flywing* we observed KL *vanishing* and solved it via *Annealing* within the first 15 epochs [1].

1.1 Run Time and Hardware Requirements

DIVNOISING using light weight fully convolutional networks (see Supplementary Figs. 1 and 2) runs on relatively cheap computational budget. Our depth 2 networks trained for all experiments requires about 1.8 GB GPU memory and our depth 3 networks roughly 5 GB GPU memory on a *NVIDIA TITAN Xp* GPU. The training time varied from 8 – 12 hours on average depending on the dataset.

2 Clustering of Solutions and Deriving the MAP Estimate

Here we provide additional details on how the cluster centers and the approximate MAP estimate of Fig. 3 (see main text) were found. We first drew 10000 sampled images from the approximate posterior as described in Section 4 of the main text. We then performed mean shift [2] clustering (using the existing *scipy* implementation) on the cropped image region shown in the figure. We set a *bandwidth* of 800 and the *maximum number of iterations* to 20, and used the 100 first samples of DIVNOISING as seeds. We finally show 9 of the resulting cluster centers in the figure.

To produce the MAP estimate, we employ a similar strategy. In order to find the mode of the sampled distribution efficiently, we assume that dependencies in the predicted samples should be local. This assumption is valid, since our network only has only a finite receptive field for each predicted pixel. Hence, we apply mean shift algorithm on locally overlapping regions. We use a window size of 10×10 pixels with an overlap of 3 pixels in x and y . On each such region, the mean shift algorithm is executed repeatedly with decreasing bandwidth, always using the latest result as new seed. We start by using the sample mean as seed and with an initial *bandwidth* of 200. After each iteration the bandwidth is decreased by a factor of 0.9, until it drops below 100.

Similar results should also be achievable by applying mean shift algorithm on the entire image. But since samples will differ at any location in the image, this global approach would require an excessively large number of DIVNOISING samples.

3 Generating Images with DivNoising Models

Just as with a standard VAE (see Section 3 in the main text), we can use a trained DIVNOISING VAE to synthesise images of structures resembling the training data. To achieve this, we sample from the normal distribution $\mathbf{z}^k \sim p(\mathbf{z})$ and process each sample with the decoder network $s^k = g_\theta(\mathbf{z}^k)$. We show such generated images in comparison to real crops from the test data in Supplementary Figs. 3 to 5. We see that the images appear most plausible for local structures, indicating that the small networks we use in this work are not capable of capturing larger structural features in the given data.

4 Instance Cell Segmentation

Here, we provide additional details regarding the downstream segmentation task described in Section 4 of the main text. We used the first 21 images in the test set of *DenoiSeg Flywing* for our analysis.

Given an input image, our segmentation pipeline consists of (i) generating segmentation masks using local thresholding with a mean filter of radius 15, followed by (ii) skeletonizing the space between these masks, followed by (iii) connected component analysis to obtain instance segmentation.

Using this pipeline, we generated segmentation for the noisy (low SNR) images, ground truth (high SNR) images, as well as for the DIVNOISING MMSE estimate (obtained by averaging 1000 sampled denoised images).

We also apply the above described pipeline for each of the 1000 DIVNOISING samples separately to serve as input for the two label fusion methods, namely (i) *Consensus (BIC)*, and (ii) *Consensus (Avg)*.

For the latter label fusion method we skip the connected component analysis and directly average the thresholded and skeletonized images. To obtain the final result, we again apply the full segmentation pipeline described above to this average image.

All segmentations were obtained with the open source image analysis software Fiji [3].

5 DivNoising vs. Denoising Variational Autoencoders

Due to their suggestive naming, we want to disambiguate DIVNOISING from *denoising variational autoencoders* [4]. Similar to DIVNOISING, Im *et al.* train VAEs using noisy input images. In contrast to us, they start with having clean images readily available. They are then adding noise to these images to improve the quality of their encoder. Additionally, their VAEs are trained using clean images in their loss function. We, on the other hand, only require noisy images during training and are interested in learning a generative model for noisy and clean images (see Eq. 9 in the main text). Hence, these two methods are, despite potentially confusing naming, fundamentally different.

6 The Relative Importance of the KL Loss Component

We can generalize our DIVNOISING training loss as a weighted combination of a modified reconstruction loss (see Eq. 10 in the main text) and KL divergence loss, where the two loss components are weighted equally. Following the exposition in [5], we explore the effect of weighting the KL loss component during training with a factor β . Our modified training loss thus becomes

$$\mathcal{L}_{\phi, \theta}(\mathbf{x}) = \mathcal{L}_{\phi, \theta}^R(\mathbf{x}) + \beta \mathcal{L}_{\phi}^{\text{KL}}(\mathbf{x}), \quad (1)$$

where setting $\beta = 1$ gives our DIVNOISING setup described in Section 4 in the main text.

Effect of β on Denoising Quality. We investigated the effect of β on the denoising ability of DIVNOISING network with the *DenoiSeg Flywing* dataset. As illustrated in Supplementary Fig. 6a, $\beta = 1$ gives the optimal results for the MMSE estimate (obtained by averaging 1000 samples). Both regimes, $\beta > 1$ and $\beta < 1$, yield sub-par denoising performance.

Effect of β on Diversity of Denoised Samples. We introduce a simple new metric, called *standard deviation PSNR*, to quantify the diversity of denoised results obtained as a function of β . For a given noisy image x and given a set of denoised samples S_x , we compute the PSNR of each sample $a \in S_x$ with respect to the corresponding ground truth image s . This yields a vector of PSNR values \mathbf{v} where $v_i = \text{PSNR}(s, a_i)$, for $v_i \in \mathbf{v}$. Standard deviation PSNR for the noisy image x is then defined as the standard deviation of elements in the vector v . Supplementary Fig. 6b reports the average of standard deviation PSNR obtained for 42 test images of the *DenoiSeg Flywing* dataset. The higher the beta, the higher is the standard deviation PSNR indicating higher diversity. Qualitative results presented in Supplementary Fig. 7 show that with $\beta > 1$, there is an increased diversity at the bigger image scales (e.g. diverse predictions of cell membranes), and generated denoised images appear smoother than those observed in real data. Setting $\beta < 1$ reduces diversity and introduces grainy artefacts, thereby yielding poor reconstructions. Note that $\beta = 1$ gives the best results in terms of PSNR of MMSE while maintaining a fair level of diversity.

Note that increasing or reducing β , *i.e.* changing the relative importance of the reconstruction loss, is equivalent to using a wider or narrower noise model, such as a Gaussian noise model with larger or smaller standard deviation σ . We can thus interpret above results as the effect of using a mismatched noise model that is either too wide or too narrow.

7 How Does Noise Affect the Diversity of DIVNOISING Samples?

We quantified how the diversity of DIVNOISING samples changes with the amount of noise present in the original dataset. Increased level of noise introduces additional uncertainty about the true signal, hence we would expect this to lead to increasingly diverse samples.

To test this hypothesis, we choose the *DenoiSeg Flywing* dataset and inject pixel wise independent gaussian noise of mean 0 and standard deviations $\sigma = 30, 50$ and 70 . We report the standard deviation PSNR diversity metric, introduced in Supplementary Section 6, for all three noise levels. As

demonstrated in Supplementary Fig. 6c, the higher the noise level, the more diverse the DIVNOISING samples become, thereby confirming our hypothesis.

8 Additional Results

More Qualitative Results. In addition to the qualitative results presented in Fig. 2 in the main text, here we present more results for each considered dataset in Supplementary Figs. 9-18.

Natural Images. We investigated the denoising performance of DIVNOISING network on the natural images benchmark dataset *BSD68* [6] and show our results in Supplementary Fig. 19. With our depth 3 network, we achieve a PSNR of 27.35 dB while our unsupervised NOISE2VOID baseline gives 27.71 dB. As discussed in the main text, this does not come as a surprise since our DIVNOISING network is comparatively small and asked to learn a complete generative model of the entire data domain (see main text and Supplementary Figs. 3-5). Learning such a model for the tremendous diversity present in natural images is challenging, and likely the reason why other architectures solving problems posed on the domain of natural images are much larger than our networks are. Future versions of DIVNOISING will address this issue by using more expressive architectures as well.

9 How Accurate is the DIVNOISING Model and the Approximate Posterior?

Upon close inspection, we find that the images sampled by DIVNOISING exhibit various imperfections, making clear that they are in fact only samples from an approximate posterior.

For example, we find that DIVNOISING samples are often smoother than real images, see *e.g.* Supplementary Figs. 9 and 16. We attribute this problem to our network architecture (see also Supplementary Section 8). For instance, a U-NET based supervised denoiser can make use of skip connections to propagate high frequency information. But DIVNOISING VAEs have to pipe all information through the downsampled latent variable bottleneck.

Another common artefact in sampled images is the presence of faint overlaid structures in the background (see Supplementary Figure 18). Note that this artefact is less pronounced than in the MMSE estimate (where we expect such artefacts).

We believe that most of these remaining issues will be solved/reduced by using more sophisticated network architectures and refined training schedules.

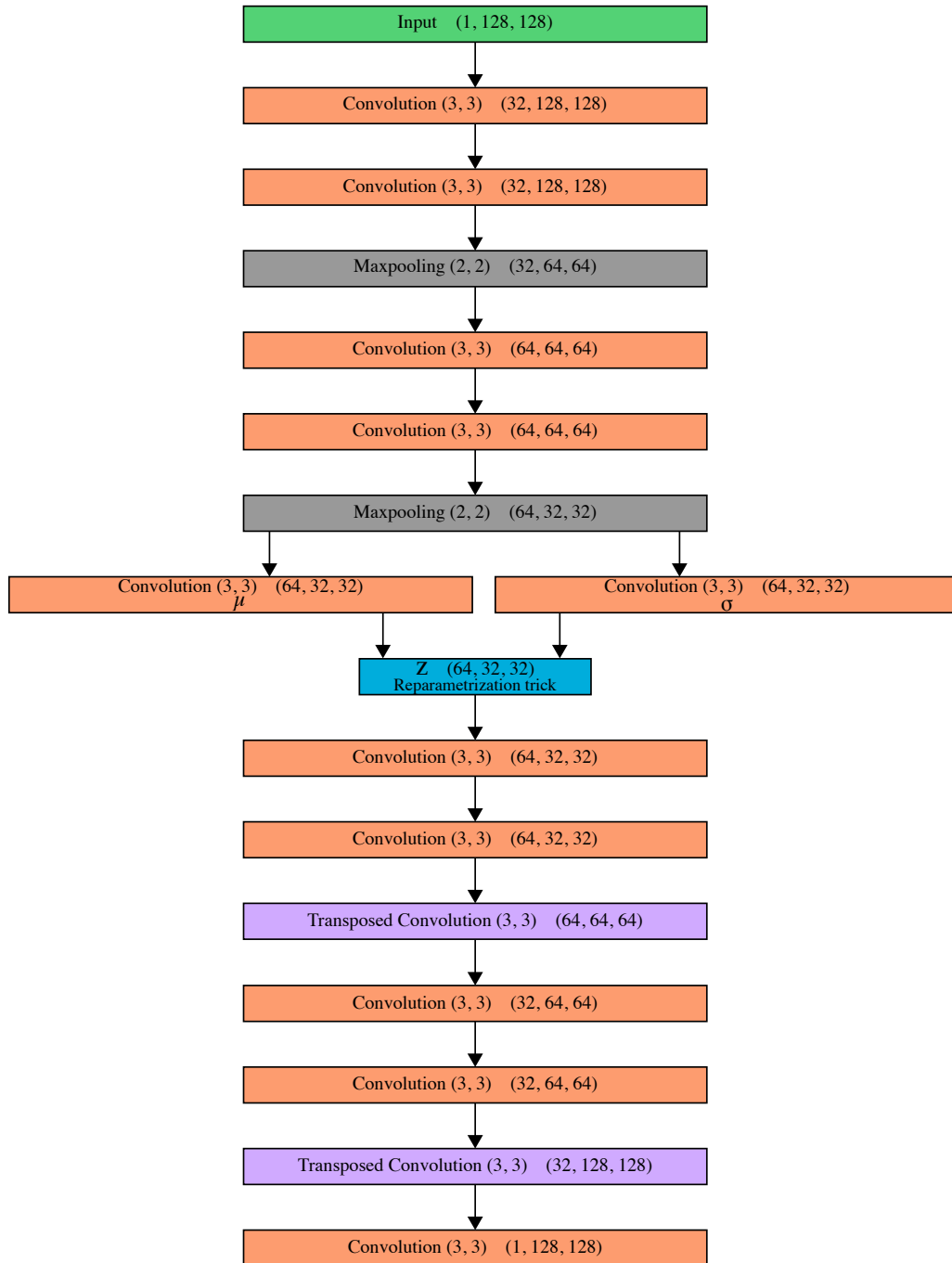


Figure 1: **The fully convolutional architecture used for depth 2 networks.** We show the depth 2 DIVNOISING network architecture used for *FU-PN2V Convallaria*, *FU-PN2V Mouse nuclei*, *FU-PN2V Mouse actin*, all *W2S* channels and *DenoISeg Mouse* datasets. These networks count about $200k$ parameters and have a GPU memory footprint of approximately 1.8GB on a *NVIDIA TITAN Xp*.

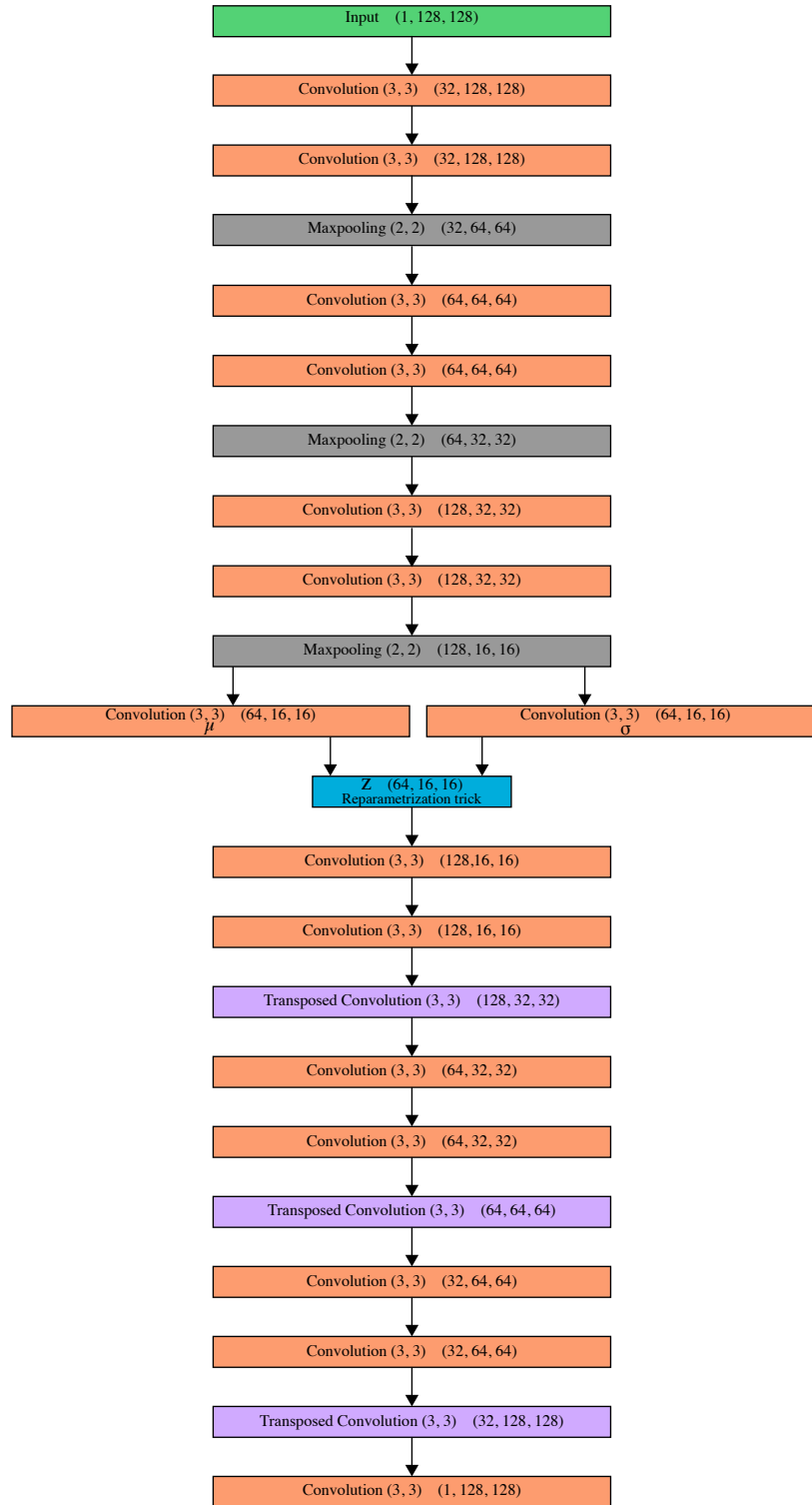


Figure 2: **The fully convolutional architecture used for depth 3 networks.** We show the depth 3 DIVNOISING network architecture used for *DenoiSeg Flywing* and *eBook* datasets. These networks count about 700k parameters and have a GPU memory footprint of approximately 5GB on a *NVIDIA TITAN Xp*.

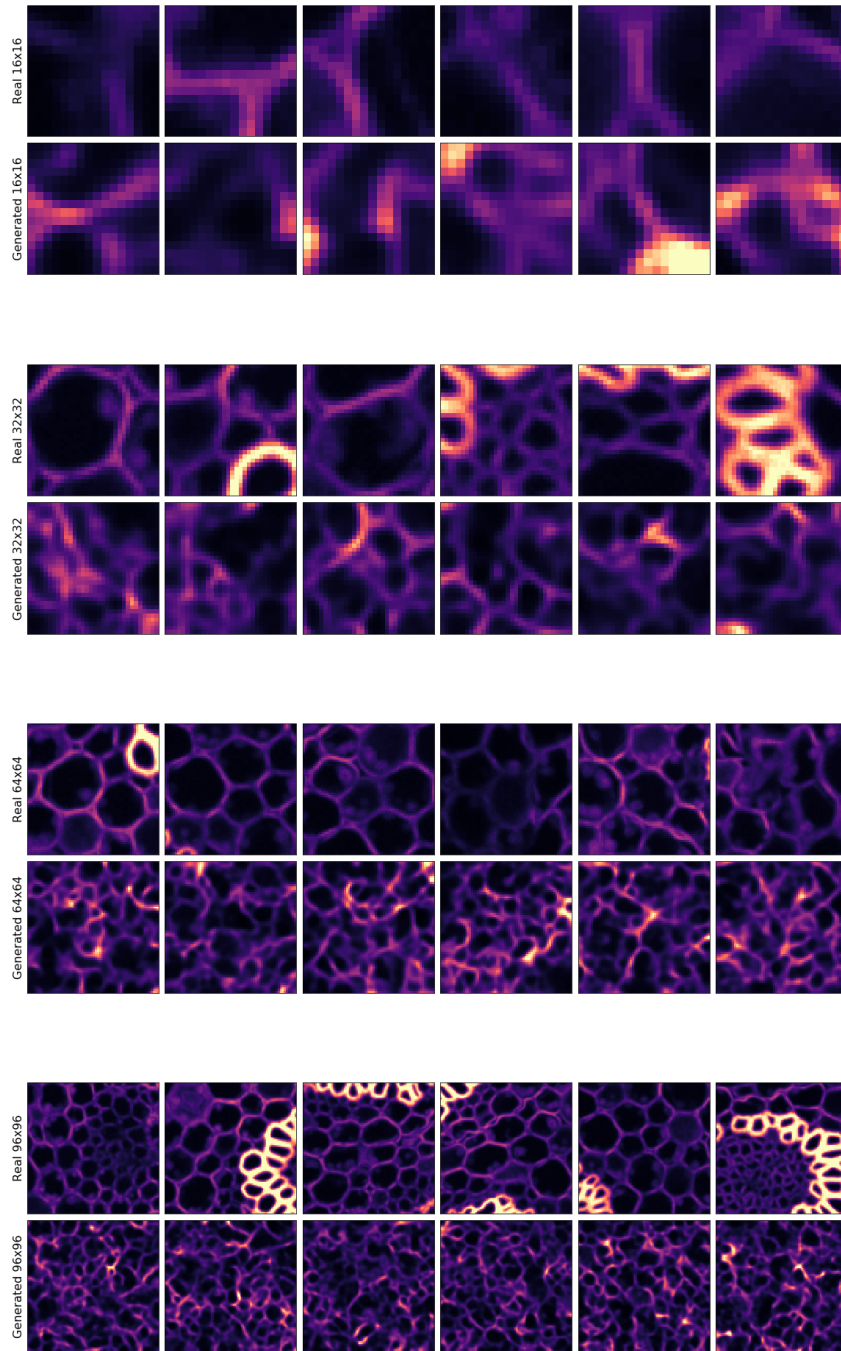


Figure 3: **Generating synthetic images with the DIVNOISING VAE for the *FU-PN2V Con-vallaria* dataset [7, 8].** DIVNOISING can also be used to generate images by sampling from the unit normal distribution $p(\mathbf{z})$ and then using the decoder to produce an image. Here, we compare generated images and randomly cropped real images. We show images of different resolutions to see how well the VAE captures structures at different scales. The VAE we use for denoising is only able to realistically capture small local structures. Note that the network we use is quite shallow (see Supplementary Fig. 1).

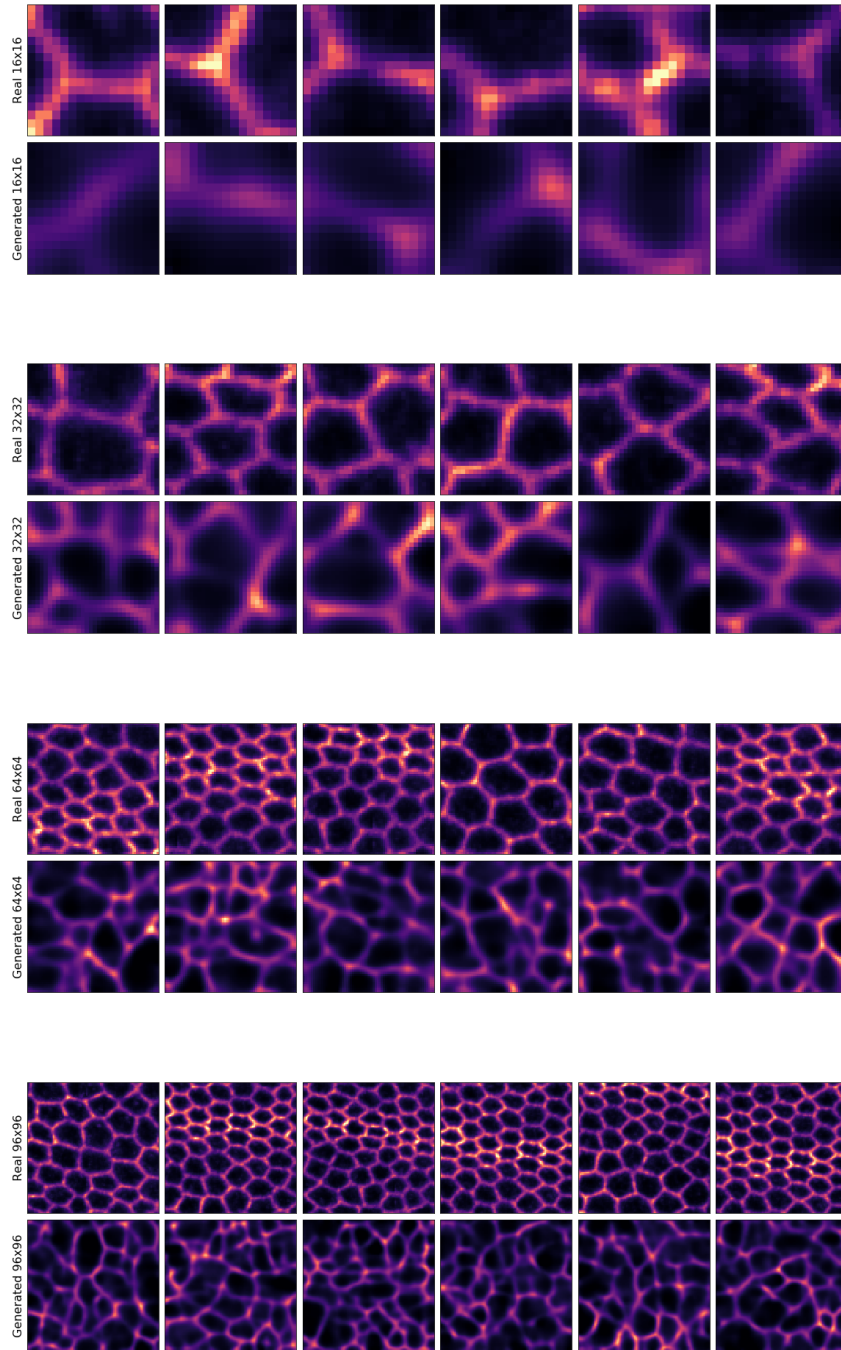


Figure 4: **Generating synthetic images with the DIVNOISING VAE for the *DenoisSeg Fly-wing* [9] dataset.** DIVNOISING can also be used to generate images by sampling from the unit normal distribution $p(\mathbf{z})$ and then using the decoder to produce an image. Here, we compare generated images and randomly cropped real images. We show images of different resolutions to see how well the VAE captures structures at different scales. Note that the network (see Supplementary Fig. 2) we use is a bit deeper compared to Supplementary Fig. 3. This VAE captures larger structures a little better but struggles to produce crisp high frequency structures. This is likely a consequence of the increased depth of the used network.

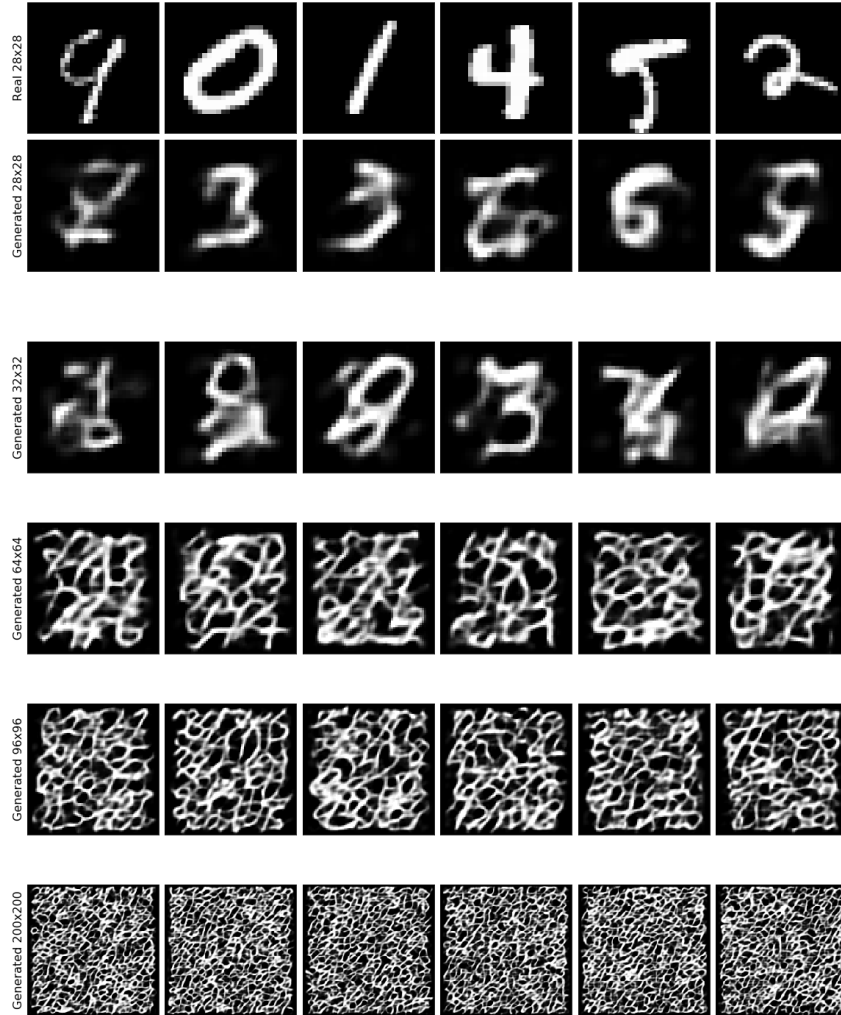


Figure 5: **Generating synthetic images with the DIVNOISING VAE for the MNIST [10] dataset.** DIVNOISING can also be used to generate images by sampling from the unit normal distribution $p(\mathbf{z})$ and then using the decoder to produce an image. Here, we compare generated images and random ground truth images. Our fully convolutional architecture allows us to generate images of different sizes (despite all input images being only of size 28×28).

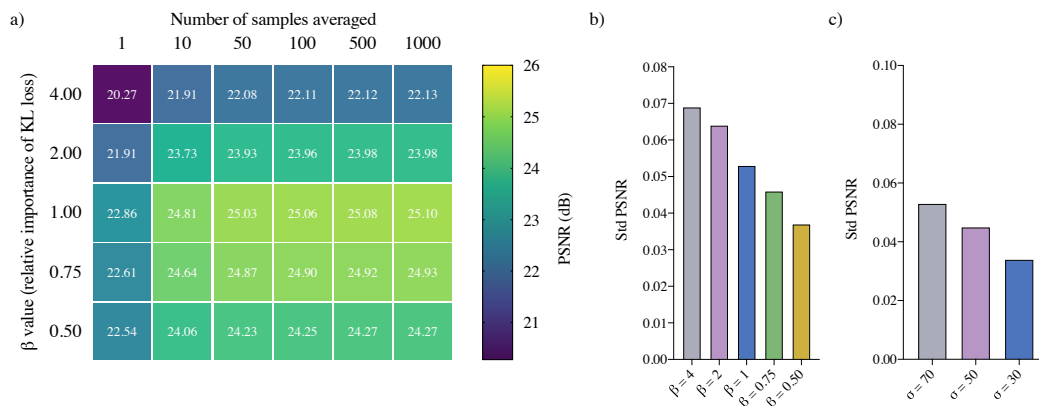


Figure 6: **Analyzing the denoising quality and diversity of DIVNOISING samples with different factors for the *DenoSeg Flywing* dataset.** (a) The heatmap shows how the quality (PSNR in db) of DIVNOISING MMSE estimate changes with averaging increasingly larger number of samples. Unsurprisingly, the more samples are averaged, the better the results get. We also investigate the effect of weighting the KL loss term with a factor β (Supplementary Eq. 1) on the quality of reconstruction. We observe that the usual VAE setup with $\beta = 1$ gives the best results in terms of reconstruction quality. Increasing $\beta > 1$ leads to higher diversity at the expense of poor reconstruction (see Supplementary Fig. 7.) (b) We quantify the denoising diversity achieved with different β values in terms of *standard deviation PSNR* (see Supplementary section 6 for details on the metric). We report the average standard deviation of PSNRs over all test images for different values of β and observe that the higher β values increase the diversity. (c) We also investigate the effect of noise on the diversity of denoised DIVNOISING samples by adding pixel wise independent zero mean Gaussian noise of standard deviations 30, 50 and 70. The higher the noise, the more ambiguous the noisy input images are, thus leading to higher diversity.

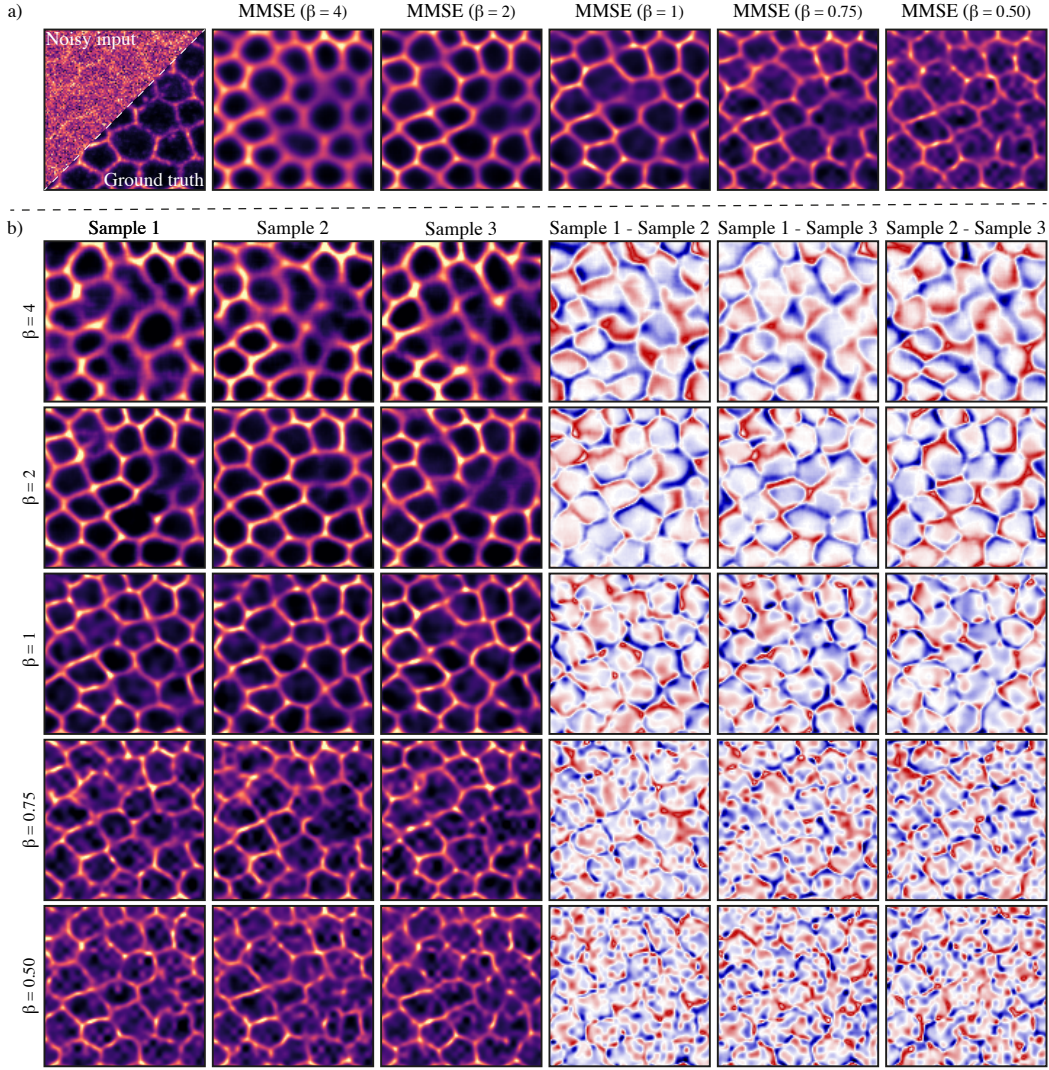


Figure 7: **Qualitative analysis of the effect of weighting KL loss term with factor β for *DenoiSeg Flying* dataset.** (a) We show the DIVNOISING MMSE estimate obtained by averaging 1000 samples for all considered β values (Supplementary Eq. 1). We observe that the reconstruction quality suffers on either increasing $\beta > 1$ or decreasing $\beta < 1$. Best results (with respect to PSNR) are obtained with $\beta = 1$, as demonstrated in Fig. 6a. (b) For each β value, we show three randomly chosen DIVNOISING samples as well as difference images. Increasing $\beta > 1$, allows the DIVNOISING network to generate structurally very diverse denoised solutions, while typically leading to textural smoothing. Decreasing $\beta < 1$ generates DIVNOISING samples with overall much reduced structural diversity, introducing reconstruction artefacts/structures at smaller scales.

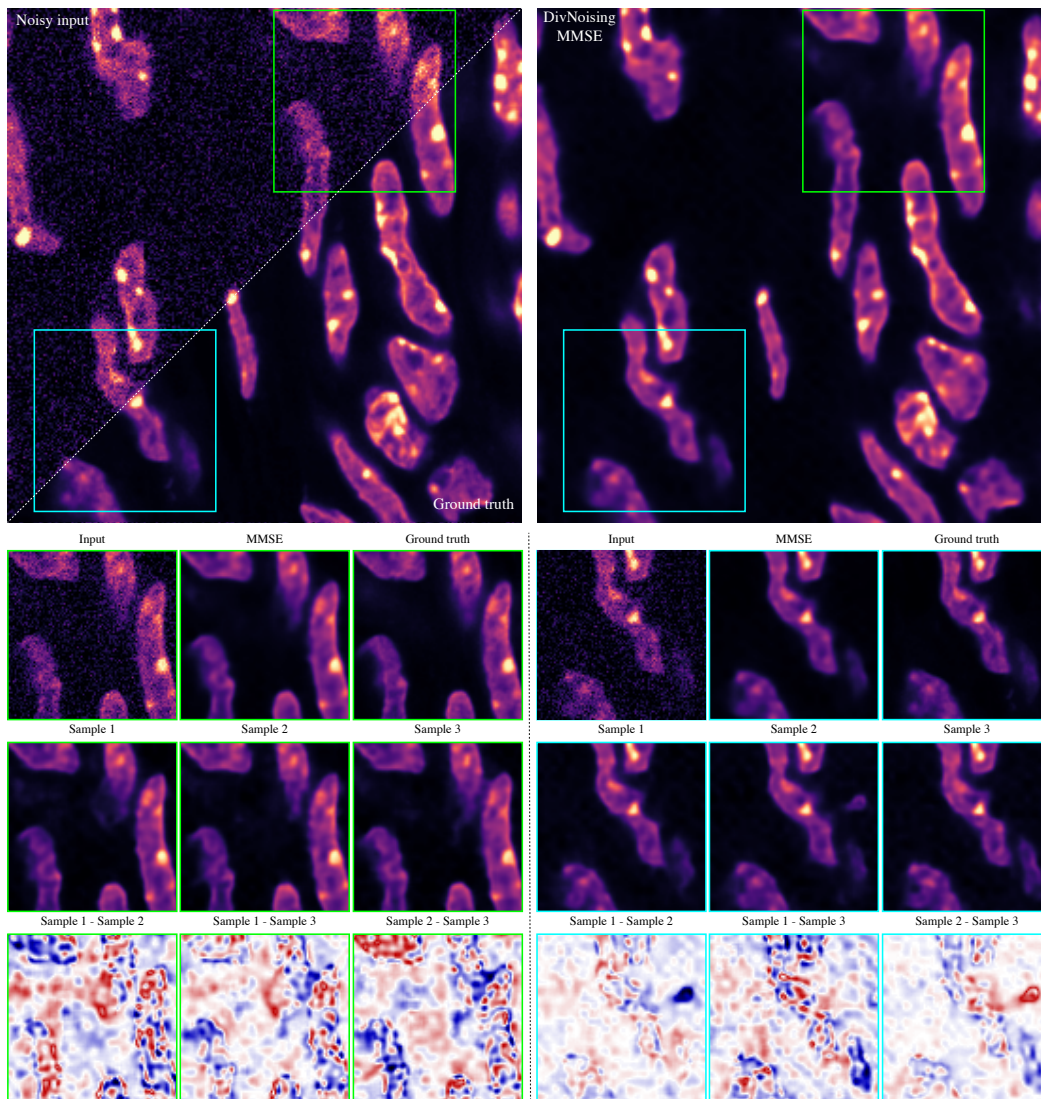


Figure 8: **Additional qualitative results for the *DenoiSeg Mouse* [9] dataset.** Here, we show qualitative results for two cropped regions (green and cyan). The MMSE estimate was produced by averaging 1000 sampled images. We choose 3 samples to display to illustrate the diversity of DIVNOISING results.

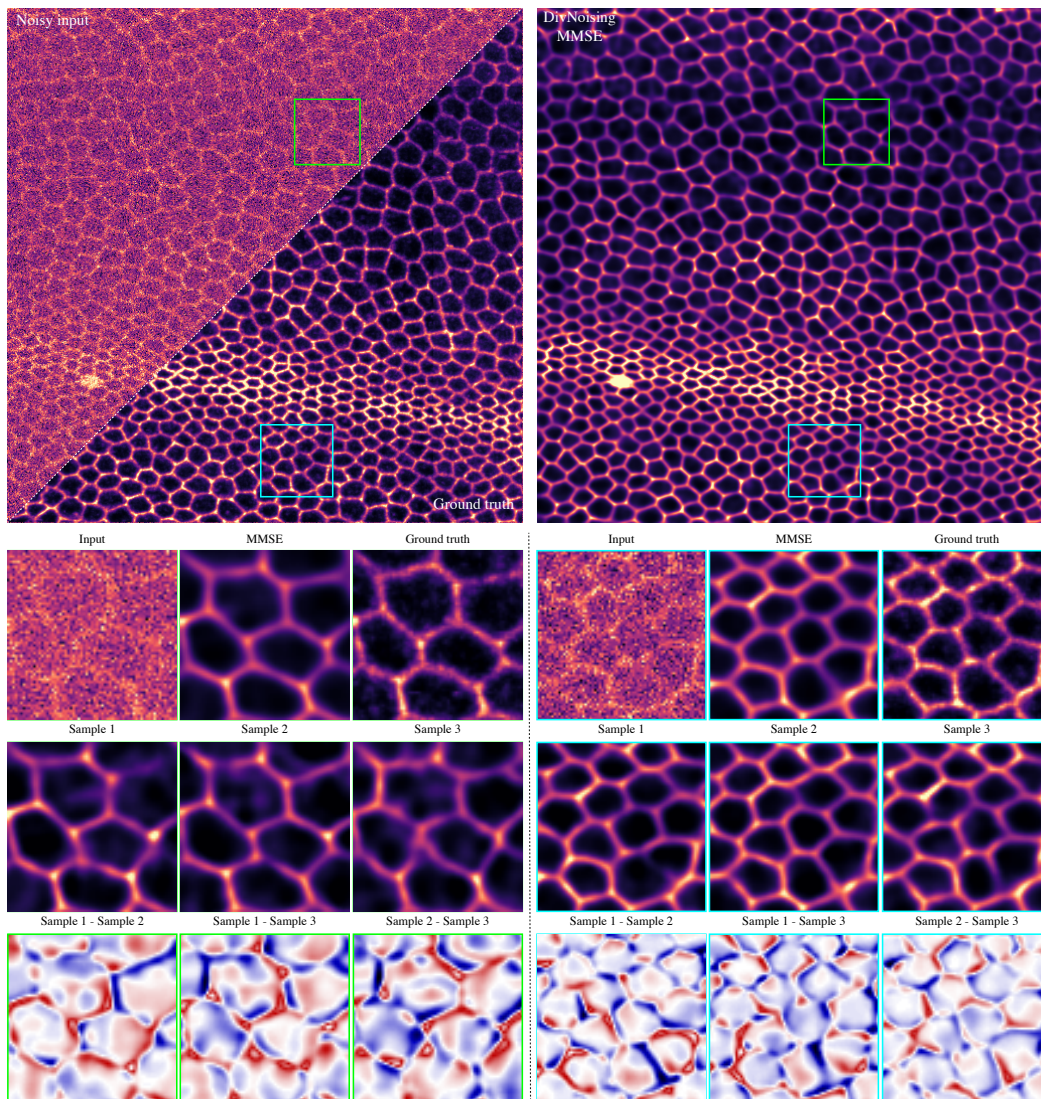


Figure 9: **Additional qualitative results for the *DenoiSeg Flywing* [9] dataset.** Here, we show qualitative results for two cropped regions (green and cyan). The MMSE estimate was produced by averaging 1000 sampled images. We choose 3 samples to display to illustrate the diversity of DIVNOISING results.

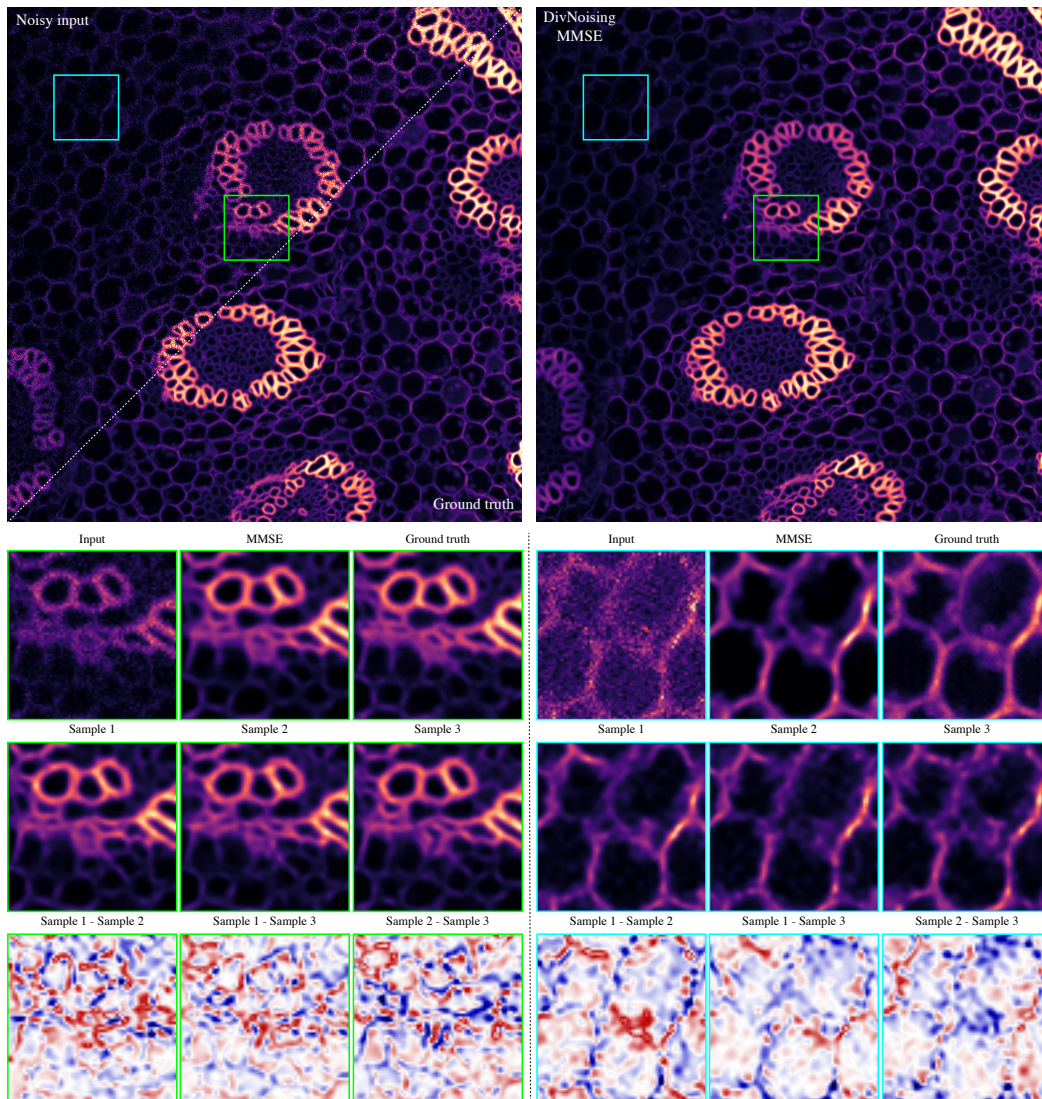


Figure 10: **Additional qualitative results for the *FU-PN2V Convallaria* [7, 8] dataset.** Here, we show qualitative results for two cropped regions (green and cyan). The MMSE estimate was produced by averaging 1000 sampled images. We choose 3 samples to display to illustrate the diversity of DIVNOISING results.

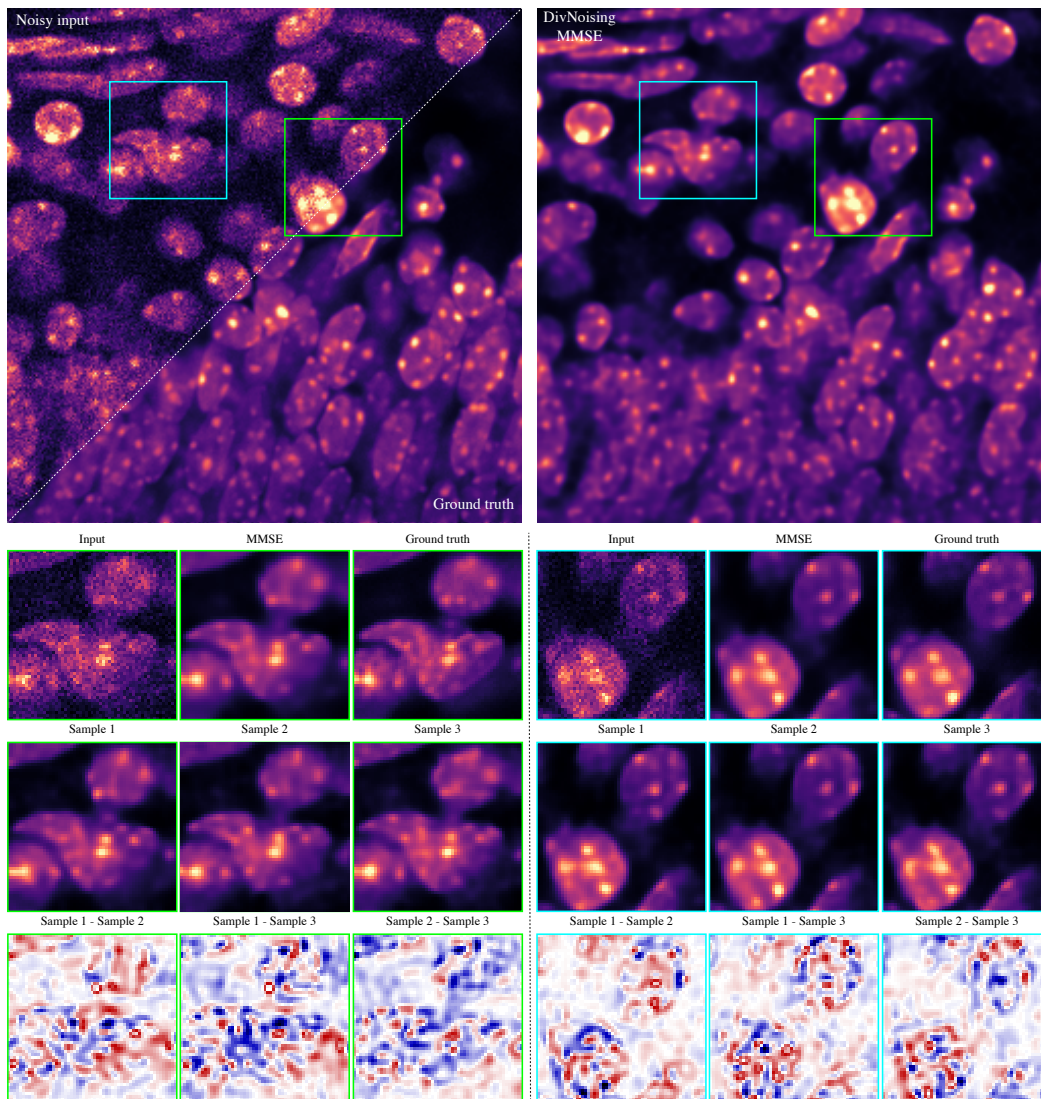


Figure 11: **Additional qualitative results for the *FU-PN2V Mouse nuclei* [8] dataset.** Here, we show qualitative results for two cropped regions (green and cyan). The MMSE estimate was produced by averaging 1000 sampled images. We choose 3 samples to display to illustrate the diversity of DIVNOISING results.

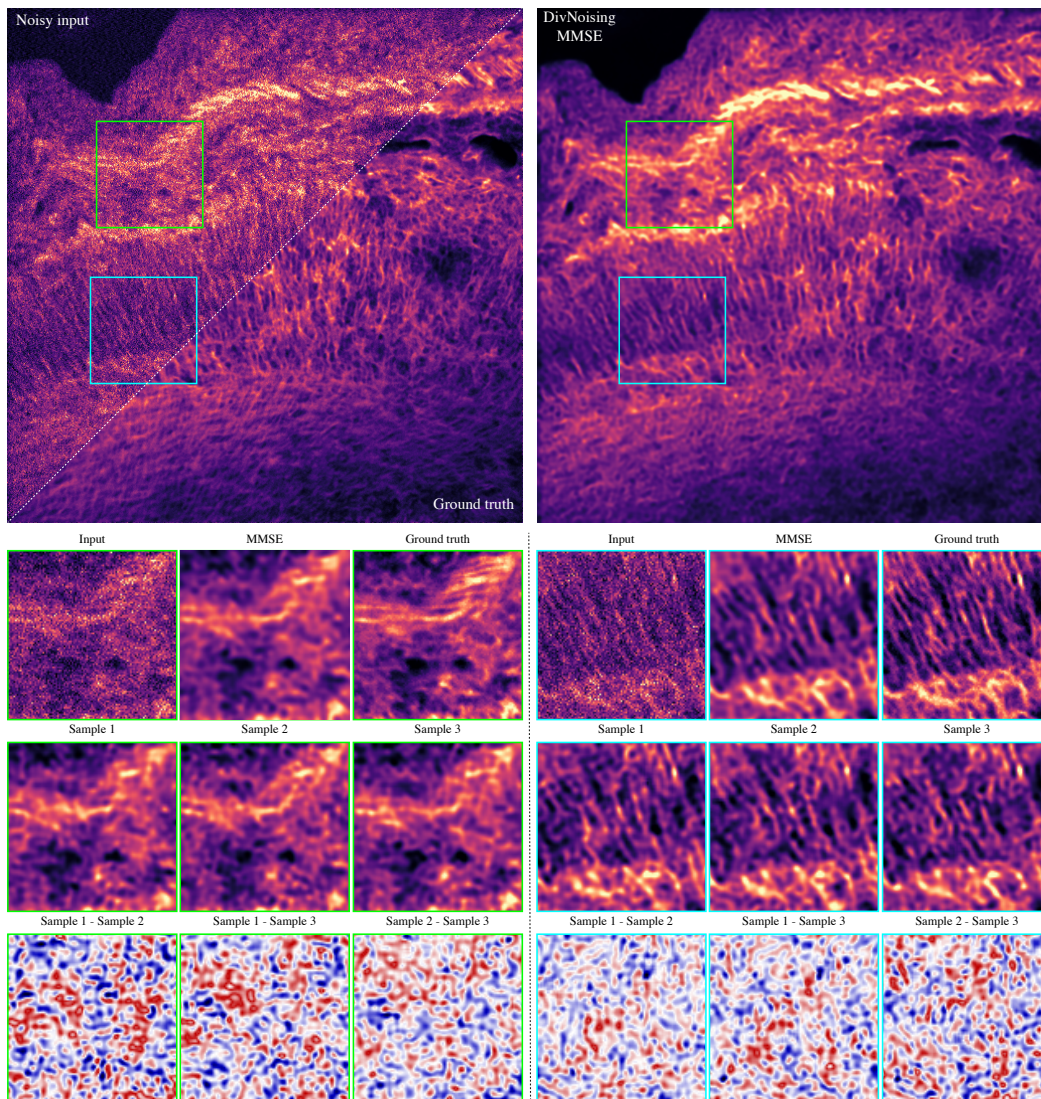


Figure 12: **Additional qualitative results for the *FU-PN2V Mouse actin* [8] dataset.** Here, we show qualitative results for two cropped regions (green and cyan). The MMSE estimate was produced by averaging 1000 sampled images. We choose 3 samples to display to illustrate the diversity of DIVNOISING results.

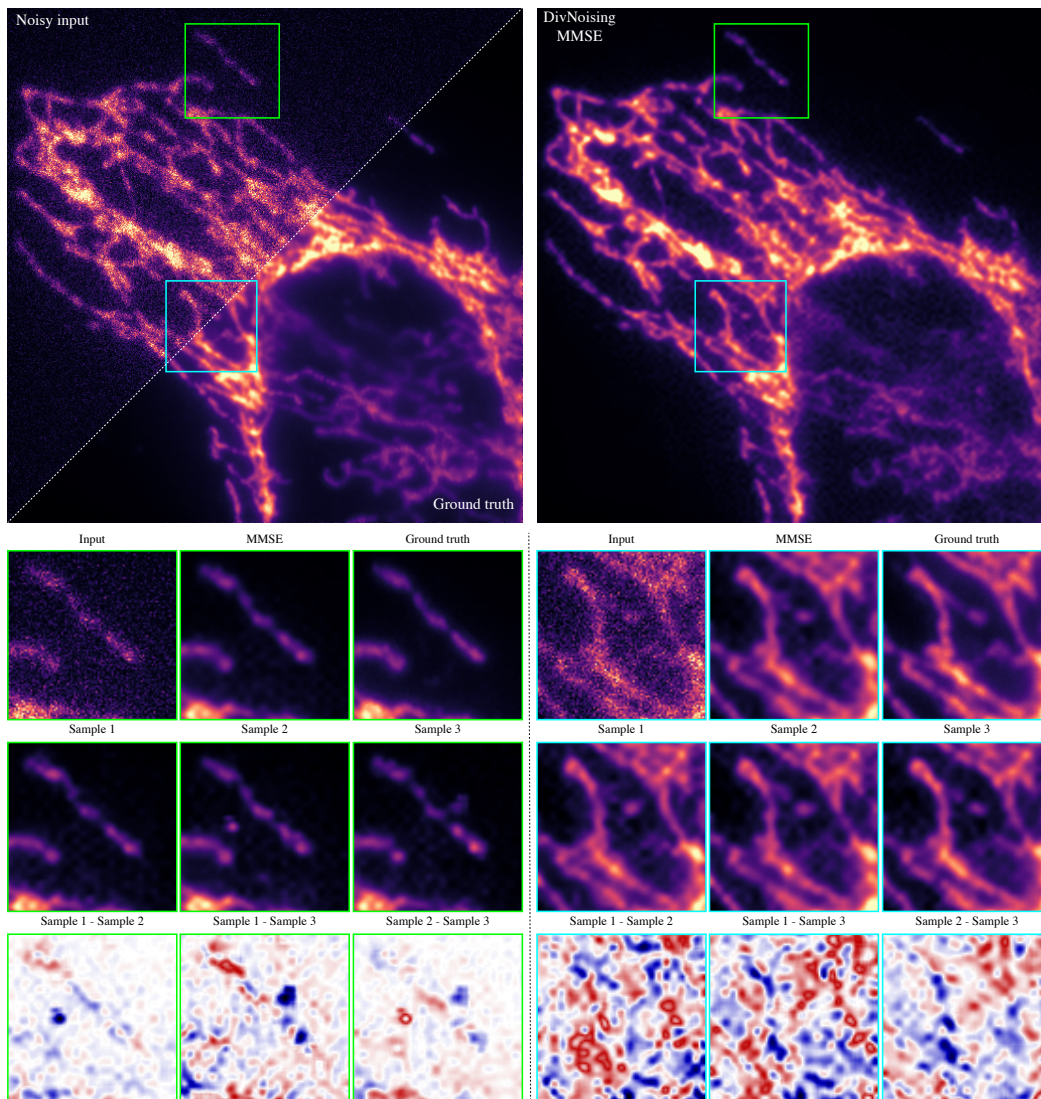


Figure 13: **Additional qualitative results for the W2S [11] dataset (ch. 0, avg1).** Here, we show qualitative results for two cropped regions (green and cyan). The MMSE estimate was produced by averaging 1000 sampled images. We choose 3 samples to display to illustrate the diversity of DIVNOISING results.

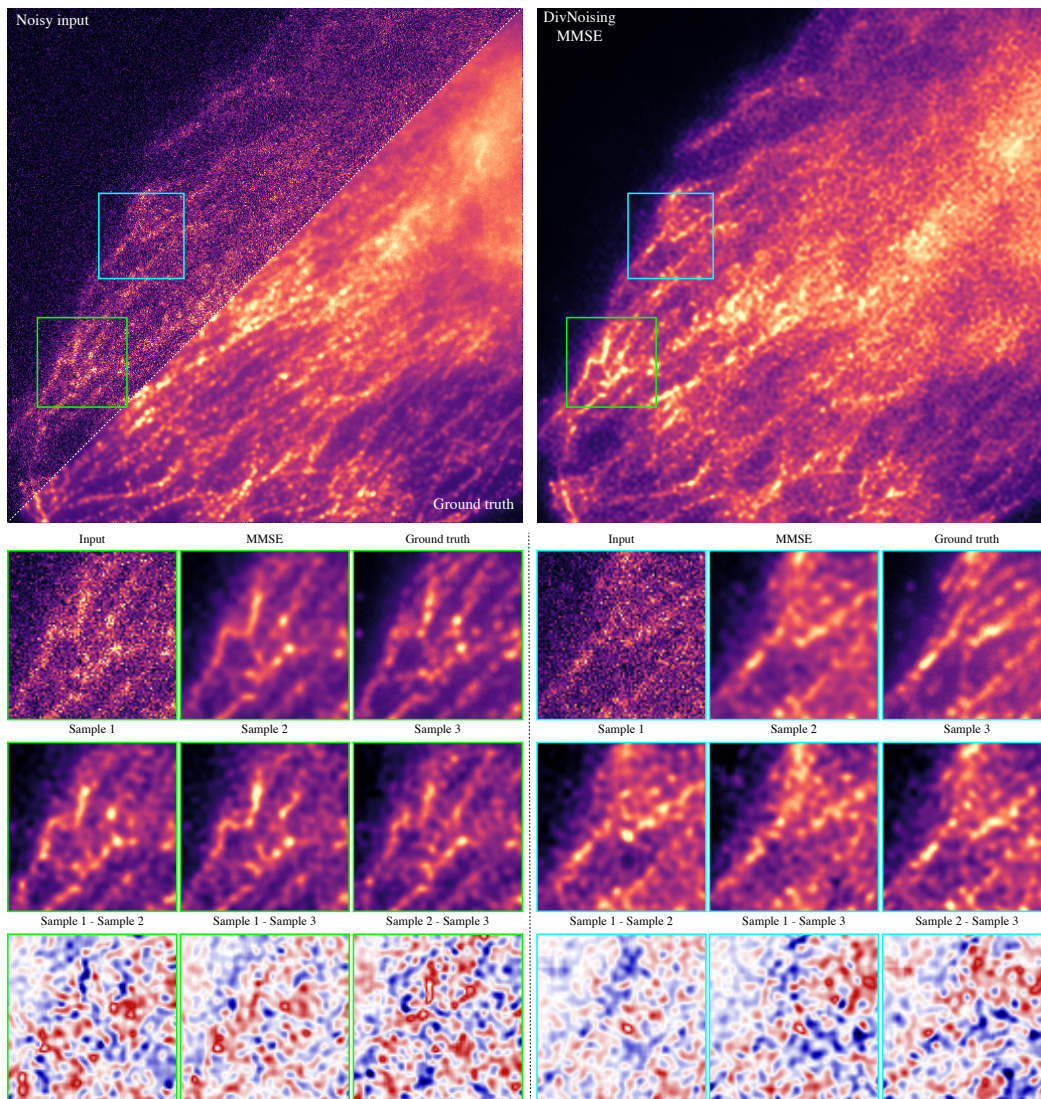


Figure 14: **Additional qualitative results for the W2S [11] dataset (ch. 1, avg1).** Here, we show qualitative results for two cropped regions (green and cyan). The MMSE estimate was produced by averaging 1000 sampled images. We choose 3 samples to display to illustrate the diversity of DIVNOISING results.

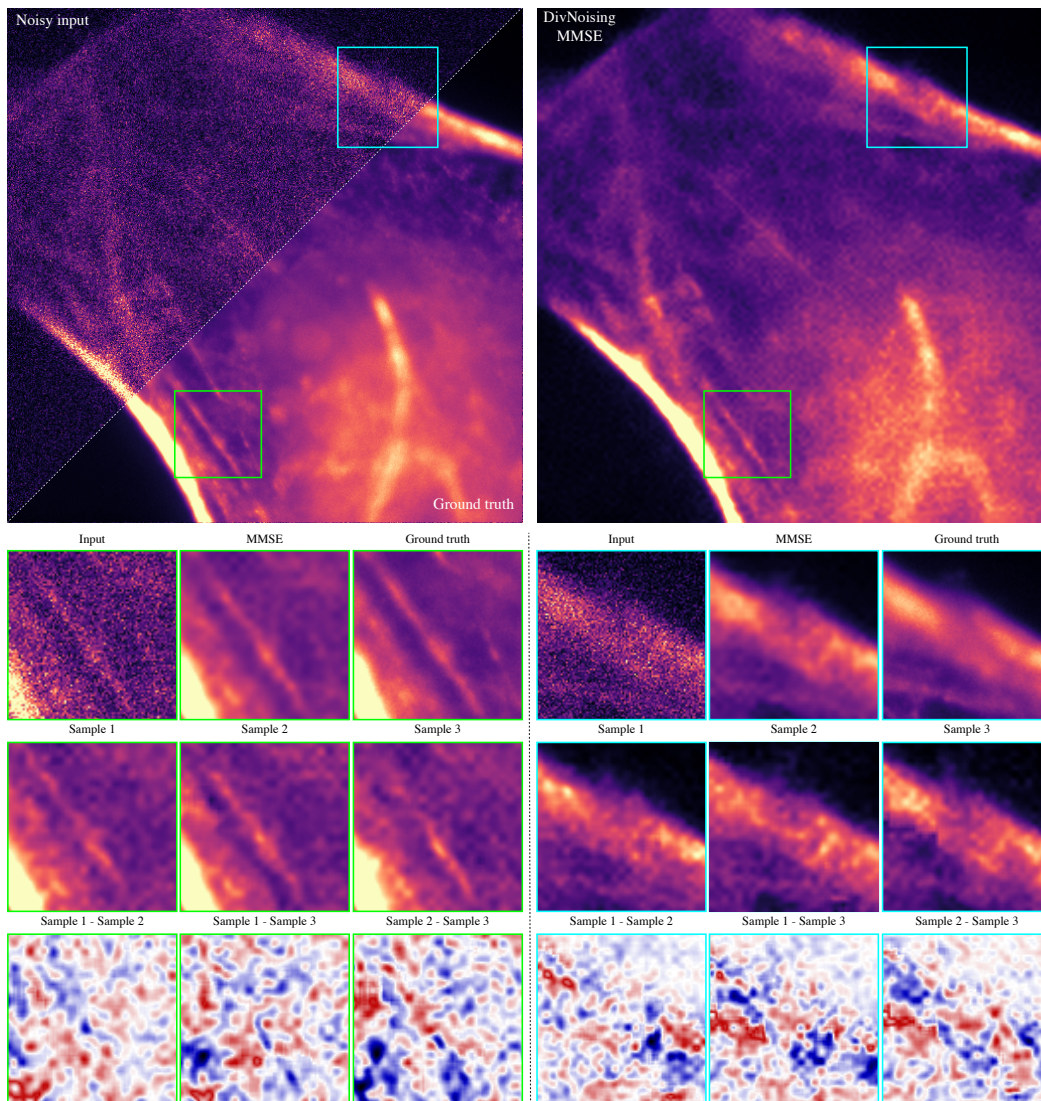


Figure 15: **Additional qualitative results for the W2S [11] dataset (ch. 2, avg1).** Here, we show qualitative results for two cropped regions (green and cyan). The MMSE estimate was produced by averaging 1000 sampled images. We choose 3 samples to display to illustrate the diversity of DIVNOISING results.

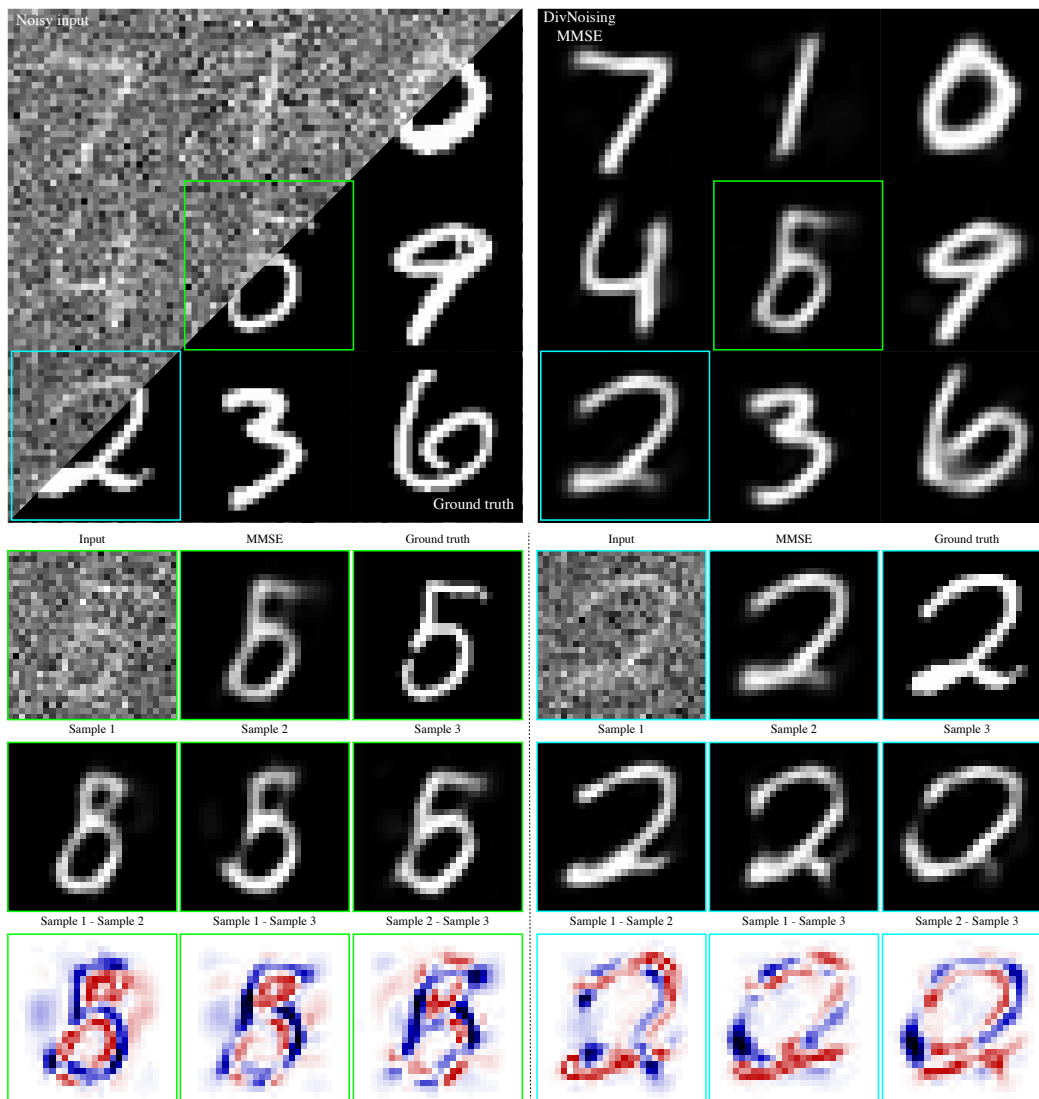


Figure 16: **Additional qualitative results for the MNIST [10] dataset.** Here, we show qualitative results for two cropped regions (green and cyan). The MMSE estimate was produced by averaging 1000 sampled images. We choose 3 samples to display to illustrate the diversity of DIVNOISING results.

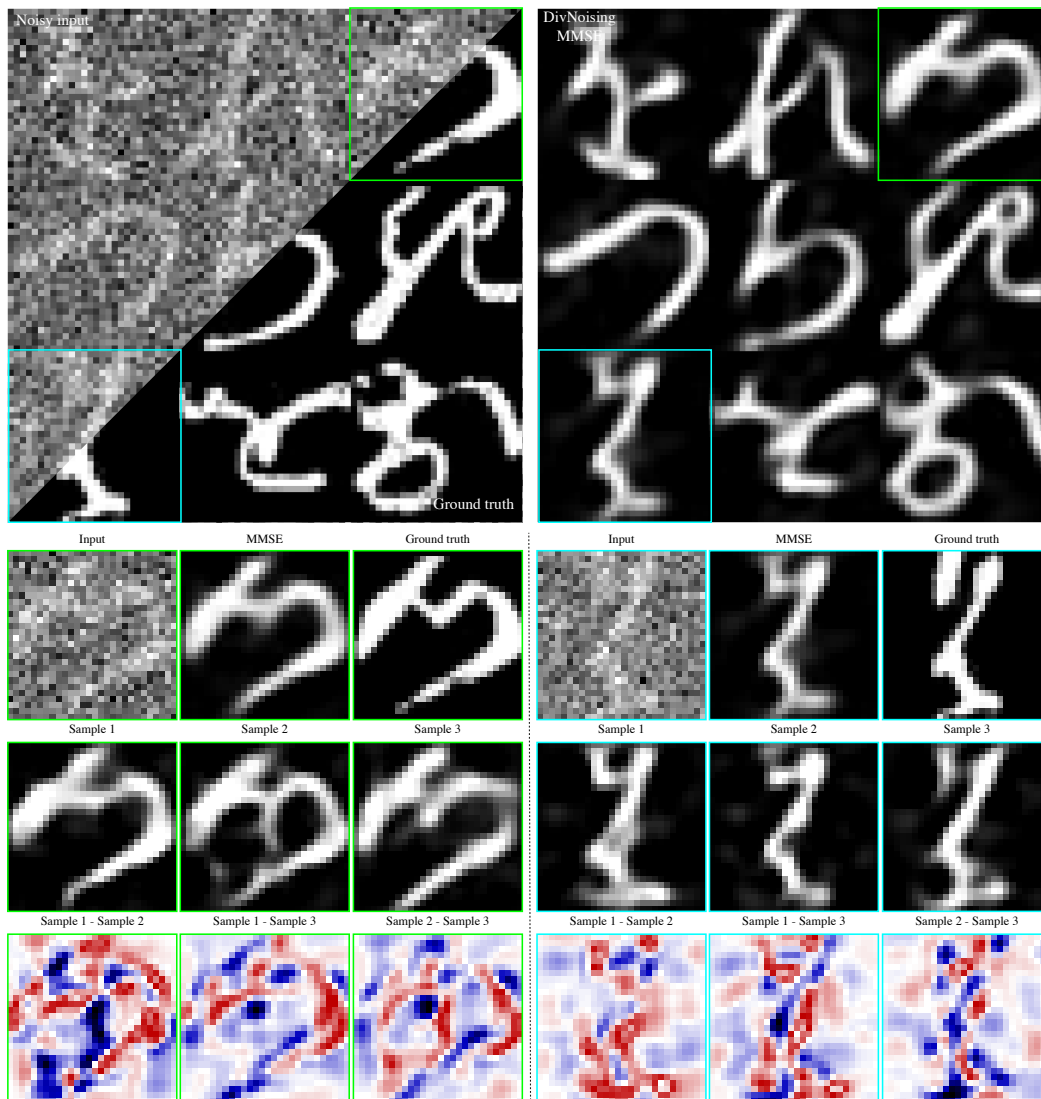


Figure 17: **Additional qualitative results for the *MNIST* [12] dataset.** Here, we show qualitative results for two cropped regions (green and cyan). The MMSE estimate was produced by averaging 1000 sampled images. We choose 3 samples to display to illustrate the diversity of DIVNOISING results.

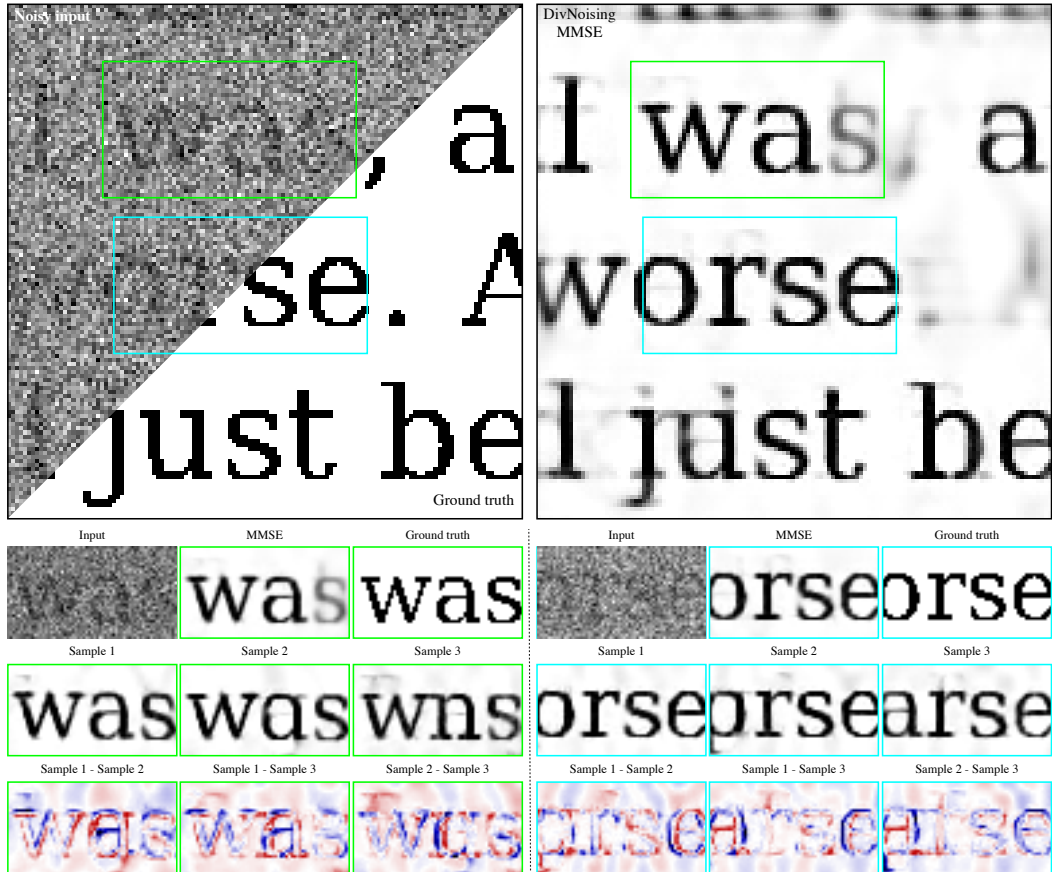


Figure 18: **Additional qualitative results for the *eBook* [13] dataset.** Here, we show qualitative results for two cropped regions (green and cyan). The MMSE estimate was produced by averaging 1000 sampled images. We choose 3 samples to display to illustrate the diversity of DIVNOISING results.

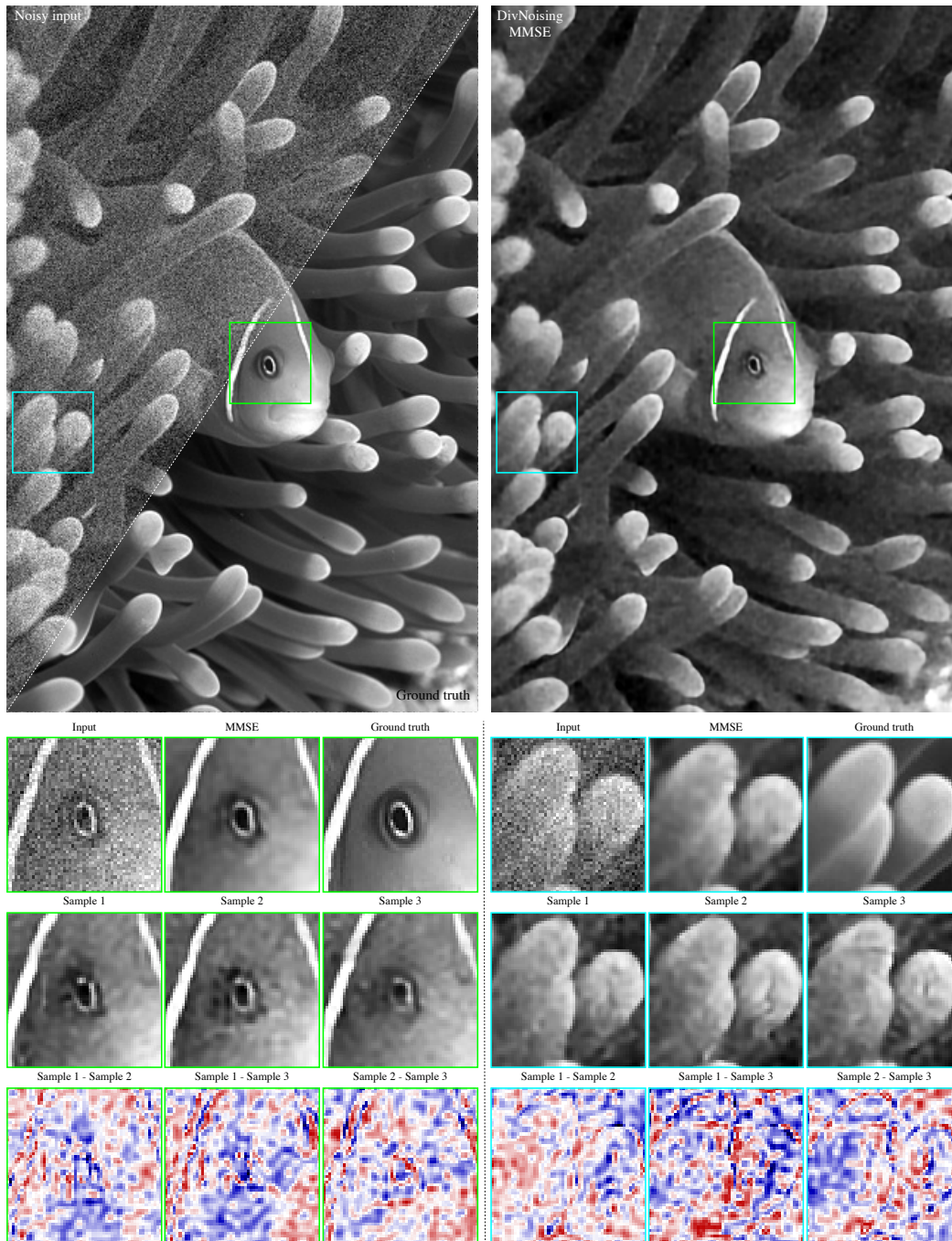


Figure 19: **Qualitative results for the *BSD68* dataset [6].** Our relatively small DIVNOISING networks fail to capture the ample structural diversity present in natural photographic images thereby exhibiting sub-par performance. However, diversity at adequately small image scales (with respect to the used network’s capabilities) can still be observed, as demonstrated with the different samples and the difference images corresponding to the green and cyan insets. We are confident that future work on DIVNOISING with larger networks and different network architectures/training schedules will expand the capabilities of this method to capture more complex image domains.

References

- [1] Samuel R Bowman, Luke Vilnis, Oriol Vinyals, Andrew M Dai, Rafal Jozefowicz, and Samy Bengio. Generating sentences from a continuous space. *arXiv preprint arXiv:1511.06349*, 2015.
- [2] Yizong Cheng. Mean shift, mode seeking, and clustering. *IEEE transactions on pattern analysis and machine intelligence*, 17(8):790–799, 1995.
- [3] Johannes Schindelin, Ignacio Arganda-Carreras, Erwin Frise, Verena Kaynig, Mark Longair, Tobias Pietzsch, Stephan Preibisch, Curtis Rueden, Stephan Saalfeld, Benjamin Schmid, Jean-Yves Tinevez, Daniel James White, Volker Hartenstein, Kevin Eliceiri, Pavel Tomancak, and Albert Cardona. Fiji: an open-source platform for biological-image analysis. *Nature Methods*, 9(7):676–682, July 2012.
- [4] Daniel Im Jiwoong Im, Sungjin Ahn, Roland Memisevic, and Yoshua Bengio. Denoising criterion for variational auto-encoding framework. In *Thirty-First AAAI Conference on Artificial Intelligence*, 2017.
- [5] Irina Higgins, Loic Matthey, Arka Pal, Christopher Burgess, Xavier Glorot, Matthew Botvinick, Shakir Mohamed, and Alexander Lerchner. beta-vae: Learning basic visual concepts with a constrained variational framework. *Iclr*, 2(5):6, 2017.
- [6] Stefan Roth and Michael J Black. Fields of experts: A framework for learning image priors. In *2005 IEEE Computer Society Conference on Computer Vision and Pattern Recognition (CVPR'05)*, volume 2, pages 860–867. IEEE, 2005.
- [7] Alexander Krull, Tomas Vicar, Mangal Prakash, Manan Lalit, and Florian Jug. Probabilistic Noise2Void: Unsupervised Content-Aware Denoising. *Front. Comput. Sci.*, 2:60, February 2020.
- [8] Mangal Prakash, Manan Lalit, Pavel Tomancak, Alexander Krull, and Florian Jug. Fully unsupervised probabilistic noise2void. *arXiv preprint arXiv:1911.12291*, 2019.
- [9] Tim-Oliver Buchholz, Mangal Prakash, Alexander Krull, and Florian Jug. Denoiseg: Joint denoising and segmentation. *arXiv preprint arXiv:2005.02987*, 2020.
- [10] Yann LeCun, Léon Bottou, Yoshua Bengio, and Patrick Haffner. Gradient-based learning applied to document recognition. *Proceedings of the IEEE*, 86(11):2278–2324, 1998.
- [11] Ruofan Zhou, Majed El Helou, Daniel Sage, Thierry Laroche, Arne Seitz, and Sabine Süsstrunk. W2s: A joint denoising and super-resolution dataset. *arXiv preprint arXiv:2003.05961*, 2020.
- [12] Tarin Clanuwat, Mikel Bober-Irizar, Asanobu Kitamoto, Alex Lamb, Kazuaki Yamamoto, and David Ha. Deep learning for classical japanese literature. *arXiv preprint arXiv:1812.01718*, 2018.
- [13] Richard Marsh. *The beetle*. Broadview Press, 2004.